nature cancer

Article

https://doi.org/10.1038/s43018-023-00626-8

A designer peptide against the EAG2–Kvβ2 potassium channel targets the interaction of cancer cells and neurons to treat glioblastoma

Received: 19 July 2022

Accepted: 2 August 2023

Published online: 11 September 2023

Check for updates

Weifan Dong[1,2,3], Adam Fekete[4], Xiaodi Chen[1,2,3], Hongwei Liu[5,6], Greg L. Beilhartz[7], Xin Chen[1,2], Shahrzad Bahrampour[1,2], Yi Xiong[1,2,5,6], Qi Yang[5,6], Hongyu Zhao[1,2,5,6], Tian Kong[4,8], Malia S. Morioka[9,10], Geena Jung[11,12], Ji-Eun Kim[1], Daniel Schramek[3,13], Peter B. Dirks[1,2,3], Yuanquan Song[11,12], Tae-Hee Kim[1,3], Ye He[9,10], Siyi Wanggou[1,2,5,6], Xuejun Li[5,6], Roman A. Melnyk[7,14], Lu-Yang Wang[4,8] & Xi Huang[1,2,3] ✉

Glioblastoma (GBM) is an incurable brain cancer that lacks effective therapies. Here we show that EAG2 and Kvβ2, which are predominantly expressed by GBM cells at the tumor–brain interface, physically interact to form a potassium channel complex due to a GBM-enriched Kvβ2 isoform. In GBM cells, EAG2 localizes at neuron-contacting regions in a Kvβ2-dependent manner. Genetic knockdown of the EAG2–Kvβ2 complex decreases calcium transients of GBM cells, suppresses tumor growth and invasion and extends the survival of tumor-bearing mice. We engineered a designer peptide to disrupt EAG2–Kvβ2 interaction, thereby mitigating tumor growth in patient-derived xenograft and syngeneic mouse models across GBM subtypes without overt toxicity. Neurons upregulate chemoresistant genes in GBM cells in an EAG2–Kvβ2-dependent manner. The designer peptide targets neuron-associated GBM cells and possesses robust efficacy in treating temozolomide-resistant GBM. Our findings may lead to the next-generation therapeutic agent to benefit patients with GBM.

Glioblastoma (GBM), the most common and aggressive primary brain cancer, leaves patients with median survival of 15–18 months[1]. Standard-of-care includes surgical resection, radiotherapy and chemotherapy using the DNA alkylating agent temozolomide (TMZ)[2]. While TMZ treatment temporarily halts tumor growth and lengthens patient survival by ~2.5 months, this is accompanied by toxicity in the neural, gastrointestinal and hematopoietic systems due to its inability to distinguish tumor and nontumoral cells. More than 50% of patients with GBM exhibit upfront or acquired TMZ resistance[3]. Furthermore, TMZ radically alters the genome of tumor cells, which promotes the emergence of therapy-resistant clones and treatment failure[4,5]. These situations necessitate the identification of druggable vulnerabilities with cancer-specific mechanisms of action, and the development of therapeutic agents to target these vulnerabilities.

Emerging evidence demonstrates that neurons are a crucial component of the tumor microenvironment. Cancer–neuron interaction promotes tumor initiation[6,7], growth[8–14], invasion[13–15] and metastasis[16]. Neurons influence tumorigenesis through both paracrine mechanisms and direct cell–cell contacts[17,18]. Neuronal activity-dependent shedding of neuroligin-3 promotes glioma cell proliferation through the PI3K–mTOR pathway in a paracrine manner[9,10]. Neurons and glioma cells form bona fide glutamatergic synapses. Action potential-induced release

A full list of affiliations appears at the end of the paper. ✉e-mail: xi.huang@sickkids.ca

of glutamate from presynaptic neurons activates calcium-permeable α-amino-3-hydroxy-5-methyl-4-isoxazolepropionic acid (AMPA) receptors on postsynaptic glioma cells, triggering calcium signaling in tumor cells that facilitates glioma proliferation and invasion[13,14]. Glioma cells form long, interconnecting cellular processes termed 'tumor microtubes'. Microtube networks underlie the malignant behavior of glioma cells, in part by propagation of calcium signaling throughout a communicating cell network[19]. Neuron–glioma synapses are enriched on glioma microtubes[13]. In turn, gliomas remodel the synaptic constituency[20] and functional neural circuits[21], inducing hyperactivity of tumor-surrounding neurons, collectively creating a protumoral microenvironment and negatively affecting patient cognition and survival. These glioma–neuron interactions underlie tumor progression and are thus emerging as an area of intense study.

Concerted membrane potential changes, which include calcium and sodium influx-dependent depolarization followed by potassium efflux-dependent repolarization, ensure continuous signal transduction from presynaptic to postsynaptic cell partners. Ion channels, which govern ionic flux across cell membrane to regulate intercellular and intracellular signaling, are key regulators in synaptic functions[22]. While ion channels comprise a large class of drug targets available to treat human diseases[23,24], the role of ion channels in glioma and glioma–neuron interactions is poorly elucidated. The potassium channel complex, which comprises both α- and β-subunits, controls potassium flux to govern cell membrane potential. α-Subunits form the potassium-conducting pore while nonconducting β-subunits physically interact with α-subunits to regulate the trafficking, stability and function of the potassium channel complex[25]. Several potassium channels that are expressed and required for in vitro GBM cell growth have been identified[26–28]. Moreover, neural activity-dependent potassium currents are frequently detected in glioma cells[13,14]. Potassium dysregulation at the glioma–brain interface contributes to aberrant neural activity and glioma hyperactivity[15]. However, how potassium channel promotes GBM growth is poorly defined. Furthermore, whether potassium channel represents a druggable node for disruption of GBM–neuron interaction and demonstrations of such a therapeutic modality remain to be firmly established. Here we report the identification of the EAG2–Kvβ2 potassium channel complex as a key regulator of GBM–neuron interaction and the development of a designer peptide to target the EAG2–Kvβ2 complex to effectively mitigate GBM.

Results

EAG2 and Kvβ2 are upregulated at the GBM–brain interface

To identify regulators of GBM–neuron interaction we interrogated the Ivy Glioblastoma Atlas Project (Ivy GAP), an anatomical transcriptomic atlas of human GBM in which RNA sequencing (RNA-seq) data from histopathologically distinct tumor regions (leading edge, infiltrating tumor, tumor core, perinecrotic zone, pseudopalisading cells around necrosis, regions with microvascular proliferation and regions with hyperplastic blood vessels) are available[29]. We found that *KCNH5*, which encodes the α-subunit of the voltage-gated potassium channel EAG2, and *KCNAB2*, which encodes the potassium channel auxiliary β-subunit Kvβ2, are enriched at the leading edge and infiltrating tumor regions (Fig. 1a), which collectively represent the GBM–brain interface conducive to GBM cell–neuron interaction[13,30]. The expression of *KCNH5* and *KCNAB2* is associated with the expression of genes involved in synaptic structure and signaling, calcium channels and glutamate receptors (Fig. 1a), suggesting a potential role for EAG2 and Kvβ2 in mediation of GBM–neuron interactions. To confirm this observation we acquired sections from multiple endpoint patient-derived orthotopic xenograft GBM tumors representing various GBM subtypes (classical, proneural and mesenchymal). We identified the GBM–brain interface in these tumors based on the Ivy GAP definition of leading edge (the outermost boundary of the tumor with disseminated tumor cells and colonies) and infiltrating tumor (the intermediate zone between leading edge and tumor core with infiltrations into normal tissues) (Fig. 1b,c and Extended Data Fig. 1a). Two additional types of GBM–brain interface in xenograft tumors are observed: invasive front, which is marked by disseminated infiltrative cells emanating from the tumor core, and defined boundary, which exhibits a clear border next to surrounding normal brain tissues (Fig. 1b). Concordant with Ivy GAP RNA-seq data (Fig. 1a), EAG2 and Kvβ2 expression is prominent in tumor cells at the GBM–brain interface, including leading edge, infiltrating tumor and invasive front (Fig. 1b,c and Extended Data Fig. 1a). Having established that GBM cells highly express EAG2 and Kvβ2 compared with nontumoral brain cells (Fig. 1b–d and Extended Data Fig. 1a), we performed coimmunostaining of EAG2, the neuronal marker Tau and the astrocyte marker glial fibrillary acidic protein (GFAP), followed by whole-slide scanning and confocal imaging. These data again demonstrate that GBM cells highly express EAG2 (Fig. 1d). Notably, both Tau^+ neuronal processes and $GFAP^+$ astrocytes are closely associated with $EAG2^+$ tumor cells (Fig. 1d and Extended Data Fig. 1a). These findings prompted us to study the function of EAG2 and Kvβ2 in GBM–brain interaction.

EAG2 and Kvβ2 regulate neuron-dependent GBM cell behavior

To this end we cocultured GBM cells with mouse primary neurons or astrocytes (Fig. 2a), the two major cell types that closely associate with tumor cells in the GBM microenvironment (Fig. 1d and Extended Data Fig. 1a)[13,14]. Intriguingly, EAG2 is prominently enriched at GBM cell–neuron or GBM cell–astrocyte contact sites, where tumor cells interact with the neurites extending from neurons (Fig. 2b) or cellular processes extending from astrocytes (Extended Data Fig. 1b). In contrast, EAG2 shows scattered localization in GBM cells that do not physically contact neurons or astrocytes (Fig. 2b and Extended Data Fig. 1b). These findings suggest that EAG2 may play a role in GBM cell–parenchymal cell interaction.

Focusing on GBM cell–neuron interaction, we sought to determine the function of EAG2 and Kvβ2 in this context using doxycycline (Dox)-inducible knockdown (Extended Data Fig. 1c). Dox-induced knockdown of Kvβ2 abrogated the enrichment of EAG2 at those regions of GBM cells in contact with neurons (Fig. 2b), demonstrating a role of Kvβ2 in mediation of neuronal contact-dependent localization of EAG2. Importantly, EAG2 colocalizes with the postsynaptic marker PSD95 in GBM cells (Fig. 2b), suggesting a role of EAG2 in perceiving neuronal inputs. Neuronal activity-dependent calcium transients in GBM cells promote their proliferation and invasion[13,14]. To determine whether EAG2 regulates the calcium dynamics of GBM cells, we performed calcium imaging of GBM cells cocultured with neurons. GBM cells expressed GCaMP6s, a genetically encoded calcium sensor, and tdTomato. Active calcium compartments were identified as subcellular regions with localized calcium transients (indicated by white arrows in Fig. 2c); *t*0–5 indicates six consecutive time points when calcium dynamics were observed (Fig. 2c,d). Dox-induced knockdown of EAG2 markedly decreased both the number of active calcium compartments and calcium activity level compared with control GBM cells (Fig. 2d). These data suggest that EAG2 and Kvβ2 may regulate neuron-dependent GBM cell behavior.

Based on this notion, we compared GBM cells in monocultures and neuron cocultures. We found that neuron coculture increases the number of GBM cells (Fig. 3a), in agreement with recent studies reporting that neuronal activity enhances glioma cell proliferation[9,10,13,14]. Dox-induced knockdown of EAG2 or Kvβ2 abrogated neuron-dependent GBM cell growth (Fig. 3a). GBM cells extend membrane protrusions to form tumor microtubes that interconnect single GBM cells to form a syncytium that promotes tumor proliferation, invasion and resistance to radiotherapy and chemotherapy[19,31]. We detected robust microtube formation (mean diameter 1.75 ± 0.73 µm, mean length 102.88 ± 46.45 µm, s.d. $n = 120$) of GBM cells in neuron cocultures (Fig. 3b). Knockdown of EAG2 or Kvβ2 decreased the percentage of GBM cells that developed microtubes and microtube length

https://doi.org/10.1038/s43018-023-00626-8

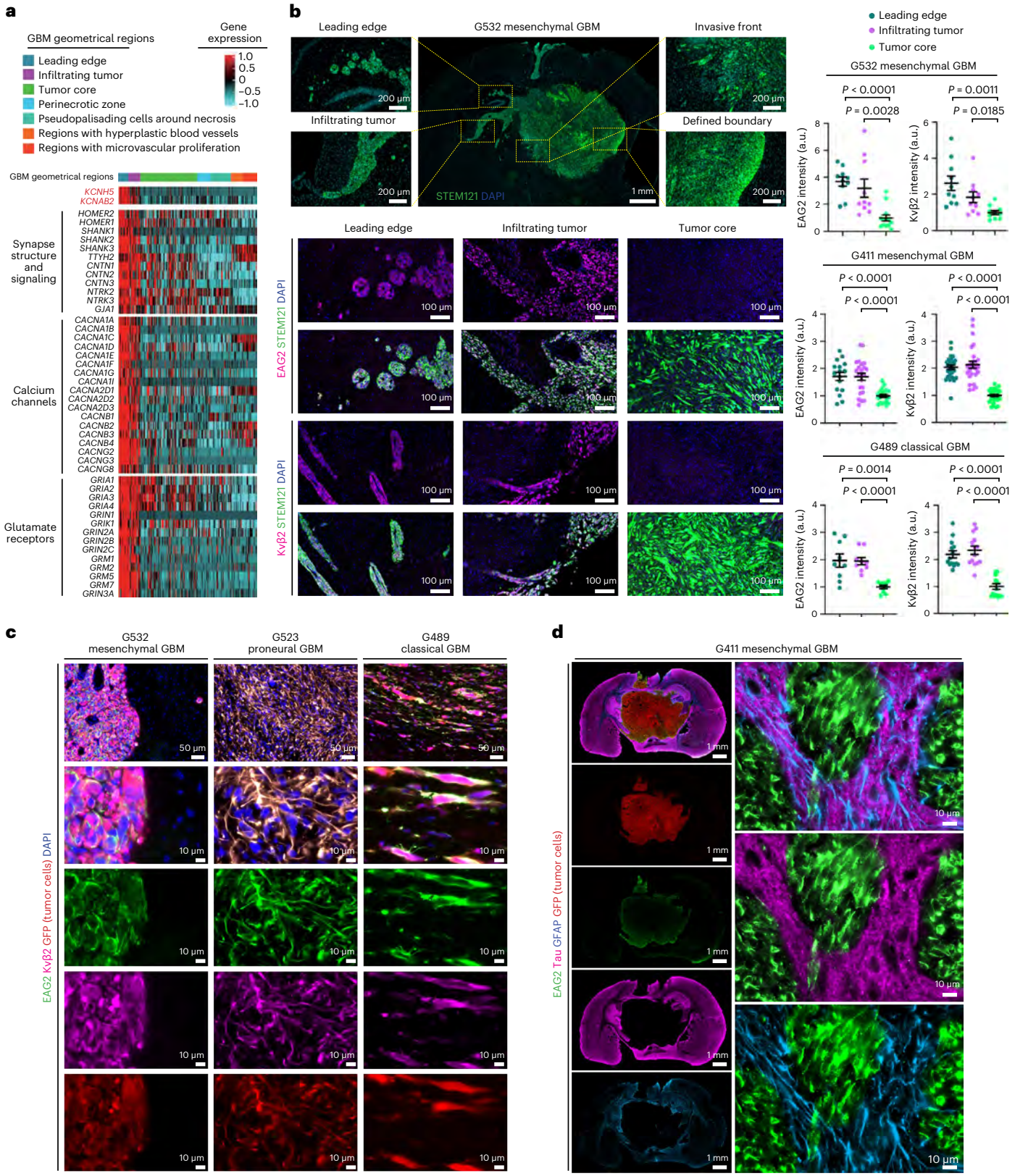

Fig. 1 | EAG2 and Kvβ2 are upregulated at the GBM–brain interface. a, Heatmap of *KCNAB2* and *KCNH5* expression in different GBM geometrical regions and their correlation with genes associated with synapse structure and signaling, calcium channels and glutamate receptors. **b**, Top left, representative images of leading edge, infiltrating tumor, invasive front and defined boundary of a G532 xenograft tumor. STEM121 detects human cell-specific cytoplasmic protein and hence was used here to label xenograft tumor cells of human origin. Bottom left, representative images of EAG2 and Kvβ2 expression in leading edge, infiltrating tumor and tumor core. Right, Quantification of EAG2 and Kvβ2 intensity per unit tumor area normalized to tumor core. Sample size (from left to right of data points for each tumor): G532, $n = 10, 10, 13, 10, 10, 10$; G411, $n = 16, 23, 20, 27, 27, 27$; G489, $n = 9, 9, 9, 14, 14, 14$ biologically independent samples from three animals were examined. *P* values, two-sided unpaired *t*-test. Error bars, mean ± s.e.m. **c**, Immunostaining of EAG2, Kvβ2 and GFP, and DAPI of G532, G523 and G489 xenograft tumors. $n = 3$ tumors examined for each GBM xenograft model. **d**, Immunostaining of EAG2, Tau, GFAP and GFP of G411 xenograft tumors. $n = 3$ tumors examined.

https://doi.org/10.1038/s43018-023-00626-8

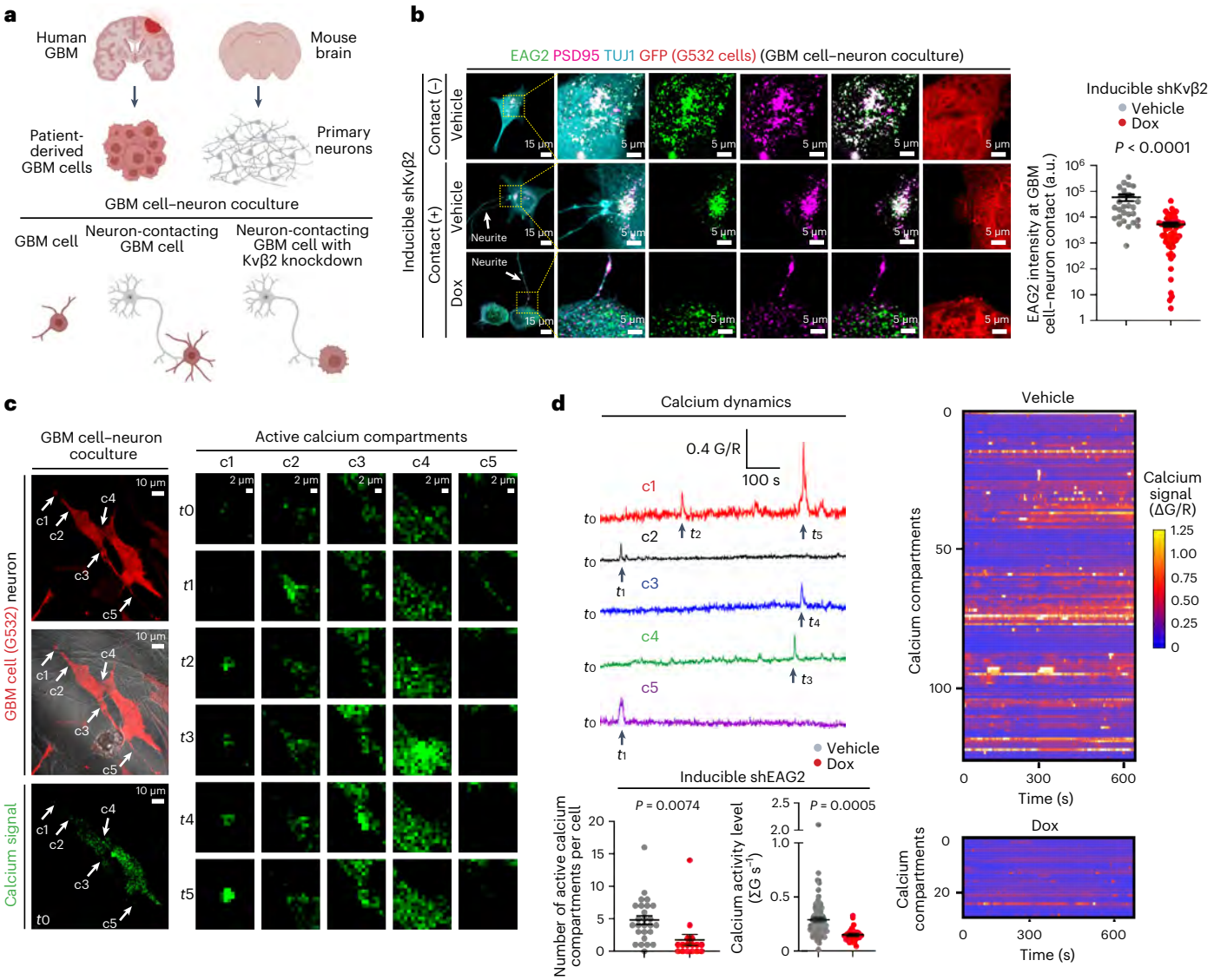

Fig. 2 | EAG2 localizes at GBM cell–neuron contact sites in a Kvβ2-dependent manner and regulates calcium transients of GBM cells. a, Schematic demonstrating the experimental procedure for GBM cell–neuron coculture. **b**, Representative images showing GFP$^+$ GBM cells without neuron contact, with neuron contact or with neuron contact and Dox-induced knockdown of Kvβ2 (shKvβ2). Green denotes EAG2 signal, magenta denotes PSD95 signal and cyan denotes TUJ1 signal, which marks both neurons and GBM cells; red (pseudocolored GFP signal) labels GBM cells. Graph shows quantification of EAG2 intensity at GBM cell–neuron contact sites. $n = 26$ cells for vehicle-treated and $n = 58$ cells for Dox-treated groups examined over three independent experiments. P values, two-sided unpaired t-test. Error bars, mean ± s.e.m. **c**, Left, representative images showing calcium signals from GCaMP6s$^+$; tdTomato$^+$ GBM cells cocultured with neurons. Right, c1–5 indicates five different active calcium compartments and $t0$–5 indicates six different time points. **d**, Top left, traces of the five different active calcium compartments expressed as G/R (G, green, GCaMP6s signal; R, red, tdTomato signal) in **c**. Bottom left, quantification of the number of active calcium compartments per cell and calcium activity level (ΣG s^{-1}) in active compartments. Active calcium compartment quantification: $n = 26$ cells for vehicle-treated and $n = 16$ cells for Dox-treated groups examined over three independent experiments. Calcium activity level per second in active compartment quantification: $n = 125$ compartments from 26 cells for vehicle-treated and $n = 28$ compartments from 16 cells for Dox-treated groups over three independent experiments were examined. P values, two-sided unpaired t-test. Error bars, mean ± s.e.m. Right, heatmap of active compartments recorded in control GBM cells and GBM cells with knockdown of EAG2 (shEAG2). $n = 117$ traces for vehicle-treated and $n = 24$ traces for Dox-treated groups are shown.

(Fig. 3b). Together, these data demonstrate that EAG2, which displays Kvβ2-dependent localization at GBM cell–neuron contact sites, modulates calcium dynamics in GBM cells. Moreover, EAG2 and Kvβ2 are required for neuron-dependent GBM cell proliferation and tumor microtube formation.

EAG2 and Kvβ2 regulate GBM growth and invasion in vivo

To determine the function of EAG2 and Kvβ2 in the regulation of GBM growth in vivo, we performed orthotopic xenograft experiments with two GBM cell lines that display distinct median survival (24 days after implantation of 2,000 G411 cells; 60 days after implantion of 100,000 G532 cells). To mimic the clinical context, we monitored the growth of xenograft tumors using noninvasive bioluminescence imaging (BLI) and initiated Dox-induced knockdown of EAG2, Kvβ2 or both only when substantial tumor burdens were detected (Fig. 3c and Extended Data Fig. 1d). Dox-induced knockdown of EAG2 or Kvβ2 mitigated tumor growth and extended survival of tumor-bearing mice (Fig. 3c and Extended Data Fig. 1d). Of note, combinatorial knockdown of EAG2 and Kvβ2 further suppressed tumor growth compared with knockdown of either gene alone (Fig. 3c and Extended Data Fig. 1d). Prompted by

the findings that EAG2 and Kvβ2 are enriched at the GBM–brain interface (Fig. 1a,b and Extended Data Fig. 1a), we examined the interface of endpoint xenograft tumors. Combinatorial knockdown of EAG2 and Kvβ2 significantly reduced infiltrating tumor colony number and size, decreased tumor boundary sinuosity (a readout for tumor invasiveness) and increased the percentage of defined boundary (Fig. 3d). Tumor cells in the leading edge, infiltrating tumor and invasive front are more likely to interact with neurons compared with tumor cells residing within a defined tumor boundary. As such, neurons interact with GBM cell microtubes to facilitate GBM cell invasion and migration[13,14,19]. We found that vehicle-treated tumors display prominent microtubes and enrichment of vesicular glutamate transporter 1 (vGlut1), an excitatory presynaptic marker, on tumor cells, highlighting GBM cell–neuron interaction in vivo (Fig. 3e). Strikingly, combinatorial knockdown of EAG2 and Kvβ2 abrogated microtube formation, led to a rounded GBM cell morphology and significantly reduced vGlut1 on tumor cells in vivo (Fig. 3e), collectively leading to a less infiltrative GBM–brain interface (Fig. 3d).

EAG2 and Kvβ2 physically and functionally interact in GBM

Having established that Kvβ2 regulates EAG2 localization at GBM cell–neuron contact regions (Fig. 2b) and that EAG2–Kvβ2 coregulates GBM malignancy (Fig. 3c and Extended Data Fig. 1d), we asked whether EAG2 and Kvβ2 physically and functionally interact. By performing coimmunoprecipitation (co-IP) using endogenous protein from patient-derived GBM cell lines, human fetal neural stem cell lines and whole mouse brains, we found that, although human fetal neural stem cells and mouse brain cells express EAG2 and Kvβ2, these two proteins exclusively interacted in tumor cells of multiple GBM subtypes, including GBM cell lines carrying mesenchymal features (G411, G532), classical features (G489), proneural features (G523)[32], mixed features (G508, G583, G799, G800)[33] and a mouse syngeneic mesenchymal cell line (GL261) (Fig. 4a,b). Because *KCNAB2* encodes five protein isoforms (Kvβ2$^{iso1–5}$; Fig. 4c), we investigated the ability of different Myc-tagged Kvβ2 isoforms to interact with EAG2. Strikingly, only Kvβ2^{iso4} interacted with EAG2 when overexpressed in HEK293T cells (Fig. 4c).

The monoclonal Kvβ2 (clone K17/70) antibody shown in Fig. 4a,b targets the epitope (amino acids (aa) 17–22) of Kvβ2^{iso1} that is absent in Kvβ2^{iso4} (Fig. 4c). Intriguingly, Kvβ2 band size (~40 kDa) indicated that Kvβ2^{iso1} (367 aa in length, ~37 kDa) interacts with EAG2 in GBM cells (Fig. 4a,b). To address this question we expressed EAG2 with Kvβ2^{iso1}, Kvβ2^{iso4} or both in HEK293T cells and performed co-IP. As expected, this Kvβ2 antibody failed to pull down Kvβ2^{iso4} in the co-IP experiment (Fig. 4d). Notably, co-IP using this Kvβ2 antibody detected both Kvβ2^{iso1} and Kvβ2^{iso4} and pulled down EAG2, demonstrating that Kvβ2^{iso4} confers EAG2-interacting ability to Kvβ2^{iso1} (Fig. 4d). Because EAG2 and Kvβ2 belong to the voltage-gated potassium channel family that contains tetramerized α- and β-subunits, our data suggest that Kvβ2^{iso1} and Kvβ2^{iso4} may form heteromultimers to interact with EAG2 in GBM cells. Strikingly, GBM cell lines—but neither nontumor nor two lung cancer cell lines—prominently express Kvβ2^{iso4} transcripts (Fig. 4e). Robust Kvβ2^{iso4} transcript expression was detected in all eight GBM cell lines studied, including those derived from six IDH wild-type primary GBM (G411, G508, G532, G583, G799, G800), one IDH mutant primary glioma (G620) and one IDH mutant recurrent GBM (G691r) (Fig. 4e). Whole-cell patch clamp recording showed that Kvβ2^{iso4} significantly increased EAG2-mediated potassium currents (Fig. 4f), indicating that Kvβ2^{iso4} functionally interacts with EAG2 to enhance its potassium channel activity.

Next, we aimed to determine the amino acid sequence of Kvβ2 that mediates its interaction with EAG2. We generated a series of Myc-tagged Kvβ2 fragment (f) mutants, cotransfected these with EAG2 fragments in HEK293T cells and performed co-IP (Fig. 4g–i). First, we truncated Kvβ2^{iso1} into three overlapping mutants: f1 (1–158 aa), f2 (79–316 aa) and f3 (239–367 aa). f1 and f2 reciprocally interacted with EAG2 (Fig. 4h,i), highlighting the necessity of their overlapping region f4 (79–158 aa). Indeed, f4 interacted with EAG2 (Fig. 4h,i). f3, or its two constituents f5 (239–316 aa) and f6 (317–367 aa), did not interact with EAG2 (Fig. 4h,i), demonstrating that the Kvβ2 C terminus does not mediate EAG2–Kvβ2 interaction. Together, these data establish that EAG2 and Kvβ2 physically interact and that Kvβ2^{iso1} amino acids 79–158 are required to mediate the formation of the EAG2–Kvβ2 complex. Kvβ2^{iso4}, but not Kvβ2^{iso1,2,3,5}, interacts with EAG2. Moreover, Kvβ2^{iso4} is prominently expressed by GBM cells but not by nontumoral cell types. Our data also suggest that amino acids 1–67, which differentiate Kvβ2^{iso1} and Kvβ2^{iso4}, may function as an autoinhibitory domain that prevents EAG2–Kvβ2 interaction.

K90-114^{TAT} disrupts EAG2–Kvβ2 interaction

The crystal structure of Kvβ2 reveals that Kvβ2 amino acids 79–158 contain two major α-helices (aa 90–114 and 126–147)[34] (Fig. 5a). We postulated that the ectopic presence of these α-helices can competitively interfere with EAG2–Kvβ2 interaction. To test this hypothesis we generated cell-penetrable peptides by the addition of a TAT cell-penetrating sequence and a linker upstream of each α-helix, which we named K90-114^{TAT} and K126-147^{TAT}, respectively (Fig. 5a). K59-78^{TAT}, a spatially adjacent α-helix of Kvβ2 (Fig. 5a), was generated as a control peptide. After treating GBM cells with each peptide, we performed co-IP to determine their ability to disrupt EAG2–Kvβ2 interaction. K90-114^{TAT}, but neither K59-78^{TAT} nor K126-147^{TAT}, reduced the interaction between endogenous EAG2 and Kvβ2 in GBM cells (Fig. 5a). To validate this observation we performed co-IP with two additional peptides as controls: K90-114 (without TAT or linker) and TAT. Again, only K90-114^{TAT} disrupted EAG2–Kvβ2 interaction, suggesting that TAT itself does not mitigate this interaction and that the cell-penetrating sequence TAT is necessary for K90-114 to disrupt EAG2–Kvβ2 interaction (Extended Data Fig. 2a). To investigate how K90-114^{TAT} affects neuron-dependent

Fig. 3 | EAG2 and Kvβ2 promote GBM growth and invasion. a, Representative images showing the number of GBM cells (green) cultured alone or with neurons (magenta) treated with vehicle or Dox. Graphs show quantification of cell number of different experimental groups shown in the images. $n = 3$ and $n = 9$ biologically independent samples were examined for Kvβ2 and EAG2 experiments, respectively. *P* values, two-sided unpaired *t*-test. Error bars, mean ± s.e.m. **b**, Representative images showing the microtubes of GBM cells (green) cultured alone or with neurons (magenta) treated with vehicle or Dox. Graphs show quantification of GBM cells with microtubes and microtube length. Sample size (from left to right of data points), $n = 10, 10, 70, 41, 10, 10, 50, 21$ biologically independent samples examined. *P* values, two-sided unpaired *t*-test. Error bars, mean ± s.e.m. **c**, Bioluminescence images showing G532 xenograft tumors before and after Dox-induced knockdown of Kvβ2, EAG2 or Kvβ2 plus EAG2. Kaplan–Meier survival curve of tumor-bearing mice is shown. Arrows denote commencement time of Dox treatment (10 days after xenograft). *P* values, log-rank test. **d**, Top, representative images of G532 xenograft tumor sections; bottom, quantifications of infiltrating tumor colony number ($n = 9$), size ($n = 9$), tumor boundary sinuosity ($n = 31$ for vehicle and $n = 28$ for Dox) and tumor boundary type percentage ($n = 9$) of vehicle- and Dox-treated tumors. Samples were evenly and independently collected from three animals. *P* values, two-sided unpaired *t*-test. Error bars, mean ± s.e.m. **e**, Representative images showing tumor microtube formation and vGlut1 expression on tumor cells in G532 xenograft tumors with vehicle or Dox treatment. Magenta denotes vGlut1 signal, green denotes STEM121 tumor signal, blue denotes nuclear DAPI signal. Graphs show quantification of invasive tumor regions with tumor microtubes ($n = 3$ tumors) and number of vGlut1 puncta on tumor cells ($n = 21$ biologically independent samples from three tumors). *P* values, two-sided unpaired *t*-test. Error bars, mean ± s.e.m. shEAG2 and shEAG2 #2 are distinct shRNAs, both targeting EAG2. The same applies to Kvβ2 shRNAs.

https://doi.org/10.1038/s43018-023-00626-8

GBM cell behavior, we performed GBM cell–neuron coculture followed by treatment of cells with K59-78^{TAT}, K90-114^{TAT}, K90-114 or TAT. K90-114^{TAT}, but not the other three peptides, decreased the number of GBM cells, the number of microtubes per GBM cell and microtube length (Fig. 5b and Extended Data Fig. 2b). Furthermore, calcium imaging showed that K90-114^{TAT}, but not K59-78^{TAT}, significantly reduced

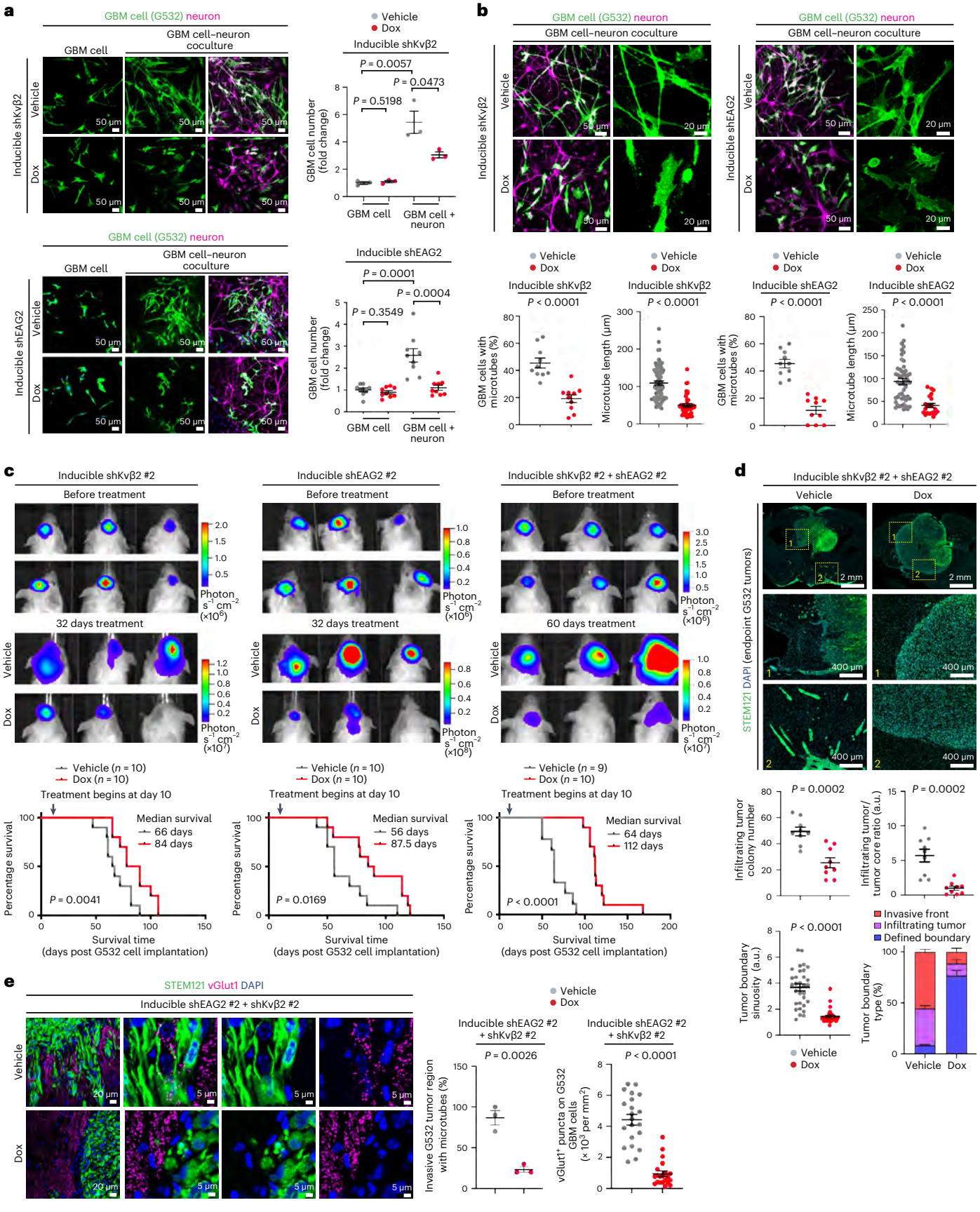

https://doi.org/10.1038/s43018-023-00626-8

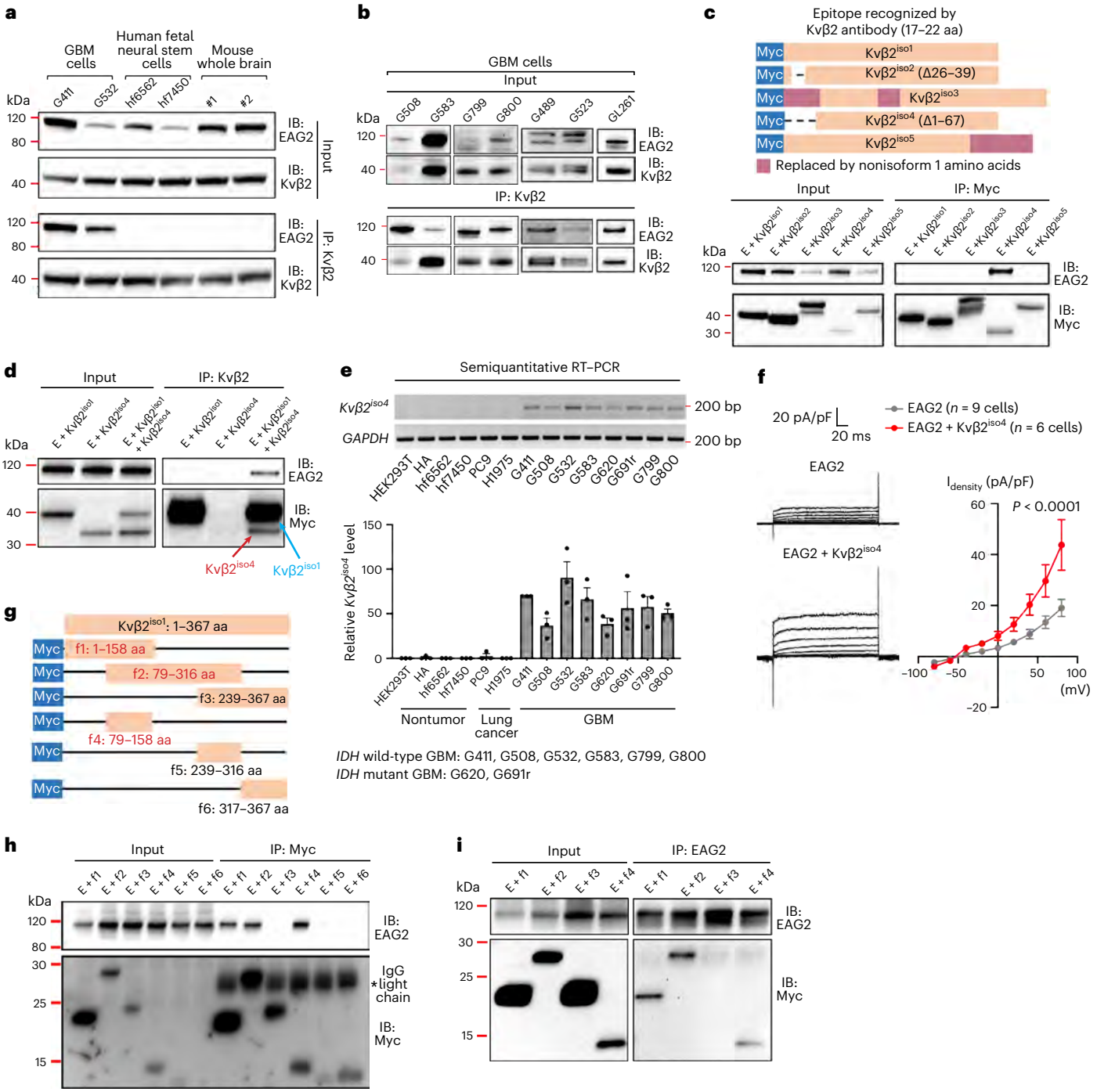

Fig. 4 | Identification of Kvβ2 amino acid sequence that mediates EAG2–Kvβ2 interaction. a, Co-IP using Kvβ2 antibody as IP antibody to detect EAG2–Kvβ2 interaction in patient-derived GBM cells, human fetal neural stem cells and mouse brains. IB, immunoblotting. **b**, Co-IP using Kvβ2 antibody as IP antibody to detect EAG2–Kvβ2 interaction in additional patient-derived and murine GBM cell lines. **c**, Schematic showing Kvβ2 isoforms and recognition by monoclonal Kvβ2 antibody of amino acids 17–22 of $Kvβ2^{iso1}$. The antibody does not recognize $Kvβ2^{iso4}$. Co-IP using Myc antibody as IP antibody to detect interaction between Myc-tagged Kvβ2 isoforms and EAG2 in HEK293T cells. E, EAG2. **d**, Co-IP using Kvβ2 antibody as IP antibody to detect interactions between EAG2 and $Kvβ2^{iso1}$, $Kvβ2^{iso4}$ and $Kvβ2^{iso1}$ + $Kvβ2^{iso4}$ in HEK293T cells. All Kvβ2 isoforms are Myc-tagged and Myc antibody is used as IB antibody. **e**, Semiquantitative PCR of Kvβ2 isoform 4 in nontumor, lung cancer and GBM cell lines. HA, human astrocytes. $n = 3$ biologically independent experiments. Error bars, mean ± s.e.m. **f**, Examples of potassium current traces evoked by voltage steps (from −80 to +80 mV in 20-mV increments, 100-ms duration) and pooled *I*–*V* curves of CHO cells transfected with EAG2 or EAG2 + $Kvβ2^{iso4}$. *P* values, two-way analysis of variance. Error bars, mean ± s.e.m. **g**, Schematic showing various Myc-tagged Kvβ2 truncation mutants studied in **h**,**i**. **h**, Co-IP using Myc antibody as IP antibody to detect interaction between Kvβ2 mutants and EAG2 in HEK293T cells. **i**, Co-IP using EAG2 antibody as IP antibody to detect interaction between Kvβ2 mutants and EAG2 in HEK293T cells. All immunolotting and qPCR were performed three times using biologically independent samples. RT–qPCR, quantitative PCR with reverse transcription. pA/pF, picoamperes per picofarad. $I_{density}$, current density.

calcium compartment number and calcium activity level (Fig. 5b). The above data indicate that K90-114^{TAT} treatment (Fig. 5b) phenocopies genetic knockdown of EAG2 or Kvβ2 in GBM cells (Figs. 2c,d and 3a,b), establishing K90-114^{TAT} as a designer peptide that disrupts EAG2–Kvβ2 interaction and suppresses GBM cell growth in vitro, prompting us to determine its in vivo anti-GBM efficacy.

https://doi.org/10.1038/s43018-023-00626-8

K90-114^{TAT} suppresses GBM growth without overt toxicity

We utilized an osmotic pump with a cannula to infuse peptide intratumorally (Fig. 5c), a delivery route that bypasses the blood–brain barrier and increases peptide local concentration. This osmotic pump-based approach is principally similar to Ommaya Reservoir, a long-term drug slow-release device used in clinics to deliver chemotherapy to patients with glioma[35]. We generated orthotopic tumor models that include various GBM subtypes (G411 mesenchymal GBM, G489 classical GBM, G523 proneural GBM) and a syngeneic immunocompetent model (GL261 mesenchymal GBM). We found that 2-week treatment of K90-114^{TAT}, but not K59-78^{TAT}, significantly suppressed GBM growth and extended the survival of tumor-bearing mice (Fig. 5d and Extended Data Fig. 2c). K90-114^{TAT} displayed anti-GBM efficacy in a dose-dependent manner (Extended Data Fig. 2d). Furthermore, we treated GBM-bearing mice with K59-78^{TAT}, TAT, K90-114 or randomized K90-114^{TAT} (in which the K90-114 amino acid sequence is randomized while maintaining the same amino acid composition). Neither TAT, K90-114 nor randomized K90-114^{TAT} treatment extended mouse survival compared with K59-78^{TAT} treatment (Extended Data Fig. 2e). These data demonstrate that the anti-GBM efficacy of K90-114^{TAT} is due neither to the general toxicity of TAT sequence nor to randomly assembled amino acids within Kvβ2 amino acids 90–114.

To determine peptide distribution we collected samples from four regions—infusion site, tumor–brain interface, hippocampus and cortex—representing regions from near to far of the infusion site (Fig. 5e). Because the osmotic pump releases peptide continuously for 14 days, we collected samples on days 4 and 14 of peptide infusion, representing the middle and end of the infusion period, respectively. Peptide concentration was then determined using liquid chromatography–mass spectrometry. At both time points, K90-114^{TAT} peptide concentrations were higher at the cannula infusion site than the tumor–brain interface. Hippocampus and cortex, two regions that are more distant from the infusion site, showed further decreased peptide concentration. These data show that designer peptide K90-114^{TAT} displays limited diffusion from the site of cannula-mediated delivery. In two out of three mice at days 4 and in three out of three mice at day 14, no peptide was detected in either hippocampus or cortex. Notably, we identified a pair of outliers in one out of three mice at day 4, in which the peptide was detected in hippocampus but not at the tumor–brain interface (Fig. 5e). We thoroughly investigated these two outlier samples. First, these two samples were retrieved from the same mouse brain. Second, because there was no accidental sample swapping, these data demonstrate that single-cannula-based peptide delivery, while effective, may not optimally deliver the peptide to a broad GBM tumor area while avoiding peptide diffusion to nontumoral brain tissue. Further development in delivery methods, such as image-guided multisite injections or placement of a peptide-releasing wafer at the tumor resection cavity, can be considered in future studies.

We further assessed the effect of peptide treatment using immunohistochemical experiments. K90-114^{TAT} treatment decreased tumor cell proliferation and increased tumor cell apoptosis (Fig. 5f,g and Extended Data Fig. 3). Of note, K90-114^{TAT}-treated tumors exhibited significantly decreased tumor microtubes and vGlut1 puncta associated with tumor cells (Fig. 5h), phenocopying tumors with genetic knockdown of EAG2 and Kvβ2 (Fig. 3e). Strikingly, K90-114^{TAT} treatment induced GBM cell apoptosis without affecting tumor-adjacent normal brain cells, even when these nontumoral cells were in closer proximity to the infusion site of K90-114^{TAT} (Fig. 5g), demonstrating that K90-114^{TAT} treatment is highly selective against GBM cells in vivo. To further determine the impact of peptide treatment on mouse physiology, we treated nontumor-bearing mice with K59-78^{TAT} or K90-114^{TAT}. K59-78^{TAT} and K90-114^{TAT}-treated mice displayed neither body weight loss nor lethality (Extended Data Fig. 4a,b). Inspections of internal organs (heart, kidney, liver, lung) did not reveal pathological features in mice treated with either peptide (Extended Data Fig. 4c).

K90-114^{TAT} targets GBM cells with neuronal features

To molecularly define those GBM cells targeted by designer peptide K90-114^{TAT}, we performed single-cell RNA-seq (scRNA-seq) on xenograft tumors treated with K59-78^{TAT} or K90-114^{TAT}. A total of 10,000 cells from three tumors for each peptide treatment were sequenced using 10X genomics. Uniform manifold approximation and projection (UMAP) clustering revealed nine distinct neoplastic cell clusters. Notably, cluster 7 GBM cells were preferentially targeted for depletion by K90-114^{TAT} (Fig. 6a). Gene Ontology (GO) biological pathway analysis showed that cluster 7 GBM cells displayed gene expression signatures conducive to GBM cell–neuron interactions, including genes that regulate neuronal projection (for example, *PTPRF*[36], *PLXNA4* (ref. 37), *VEGFA*[38] and *BDNF*[39]), axonogenesis (for example, *LRP1* (ref. 40), *VEGFA*[38] and *EPHA4* (ref. 41)), neuron migration (for example, *NAV1* (ref. 42), *MEF2C*[43] and *FGFR1* (ref. 44)) and axon regeneration (for example, *LRP1* (ref. 40), *EPHA4* (ref. 41) and *SPP1* (ref. 45)) (Fig. 6a,b).

Having identified cluster 7 as the GBM cell population targeted by K90-114^{TAT}, we investigated the clinical significance of this tumor cell population in human glioma by interrogation of The Cancer Genome Atlas low-grade glioma-GBM (LGG-GBM) dataset ($n = 607$) (Fig. 6c). Cluster 7 signature is enriched in high-grade glioma (WHO Grades 3 and 4) compared with LGGs (WHO Grade 2). While cluster 7 signature was detected across transcriptomic and molecular subtypes of gliomas, the highest cluster 7 signature was present in mesenchymal GBM that portends the worst prognosis[46] (Fig. 6c). Histologically, high cluster 7 signature is detected in GBM and astrocytoma and

Fig. 5 | K90-114^{TAT} disrupts EAG2–Kvβ2 interaction and suppresses GBM growth. a, Three-dimensional structure of Kvβ2 from Protein Data Bank (PDB no. 3eau). Colored structures indicate the sequences of three α-helices, based on which designer and control peptides were generated. Each peptide is linked with the cell-penetrating sequence TAT. Co-IP shows EAG2–Kvβ2 interaction in G532 GBM cells with K90-114^{TAT}, K59-78^{TAT} or K126-147^{TAT} treatment. **b**, Number of active calcium compartments per cell ($n = 9$ and $n = 13$ biologically independent cells), calcium activity level per second ($n = 39$ and $n = 19$ independent calcium compartments), cell number ($n = 42$ and $n = 43$ biologically independent samples) and microtube length of GBM cells ($n = 146$ and $n = 49$ biologically independent cells) cocultured with neurons following K59-78^{TAT} or K90-114^{TAT} treatment, respectively. *P* values, two-sided unpaired *t*-test. Error bars, mean ± s.e.m. **c**, Schematic showing osmotic pump-mediated, cannula-guided delivery of peptide directly into GBM in mice. **d**, Bioluminescence images showing tumor burdens before and after peptide treatment. Kaplan–Meier survival curve of tumor-bearing mice is shown. *P* value, log-rank test. **e**, Schematic showing tissue sample retrieval sites following osmotic pump-mediated, cannula-guided delivery of peptide directly into GBM in mice. Liquid chromatography–mass spectrometry showing relative peptide concentration at day 4 or 14 after commencement of peptide infusion. $n = 3$ biologically independent animals. Error bars, mean ± s.e.m. **f**, Immunostaining of tumors treated with designer peptide K90-114^{TAT} and control peptide K59-78^{TAT}. Xenograft tumor cells labeled by STEM121 (green); mitotic cells labeled by phospho-histone H3 (pHis3, magenta); apoptotic cells labeled by cleaved caspase-3 (magenta). Graphs show quantification of mitotic cells ($n = 8$ and $n = 7$ biologically independent samples from three animals) and apoptotic cells ($n = 10$ biologically independent samples from three animals) within tumors. *P* values, two-sided unpaired *t*-test. Error bars, mean ± s.e.m. **g**, Representative images showing tumor–brain interfaces from two K90-114^{TAT}-treated tumors. **h**, Tumor microtube formation, tumor cell infiltration at invasive front and number of vGluT1 puncta on tumor cells following K59-78^{TAT} or K90-114^{TAT} treatment. Graphs show quantification of tumor cells with microtubes in the invasive front ($n = 3$ biologically independent animals) and vGlut1 puncta on tumor cells ($n = 19$ and $n = 21$ biologically independent samples from three animals). *P* values, two-sided unpaired *t*-test. Error bars, mean ± s.e.m.

https://doi.org/10.1038/s43018-023-00626-8

less frequently in oligodendroglioma or oligoastrocytoma (Fig. 6c). Molecularly, high cluster 7 signature is associated with gliomas exhibiting wild-type IDH and chromosome 1p/19q noncodeletion, which are biomarkers for more aggressive glioma (Fig. 6c). In accordance, higher cluster 7 signature score is prognostic for worse survival in patients with glioma (Fig. 6d). One major reason for TMZ resistance is

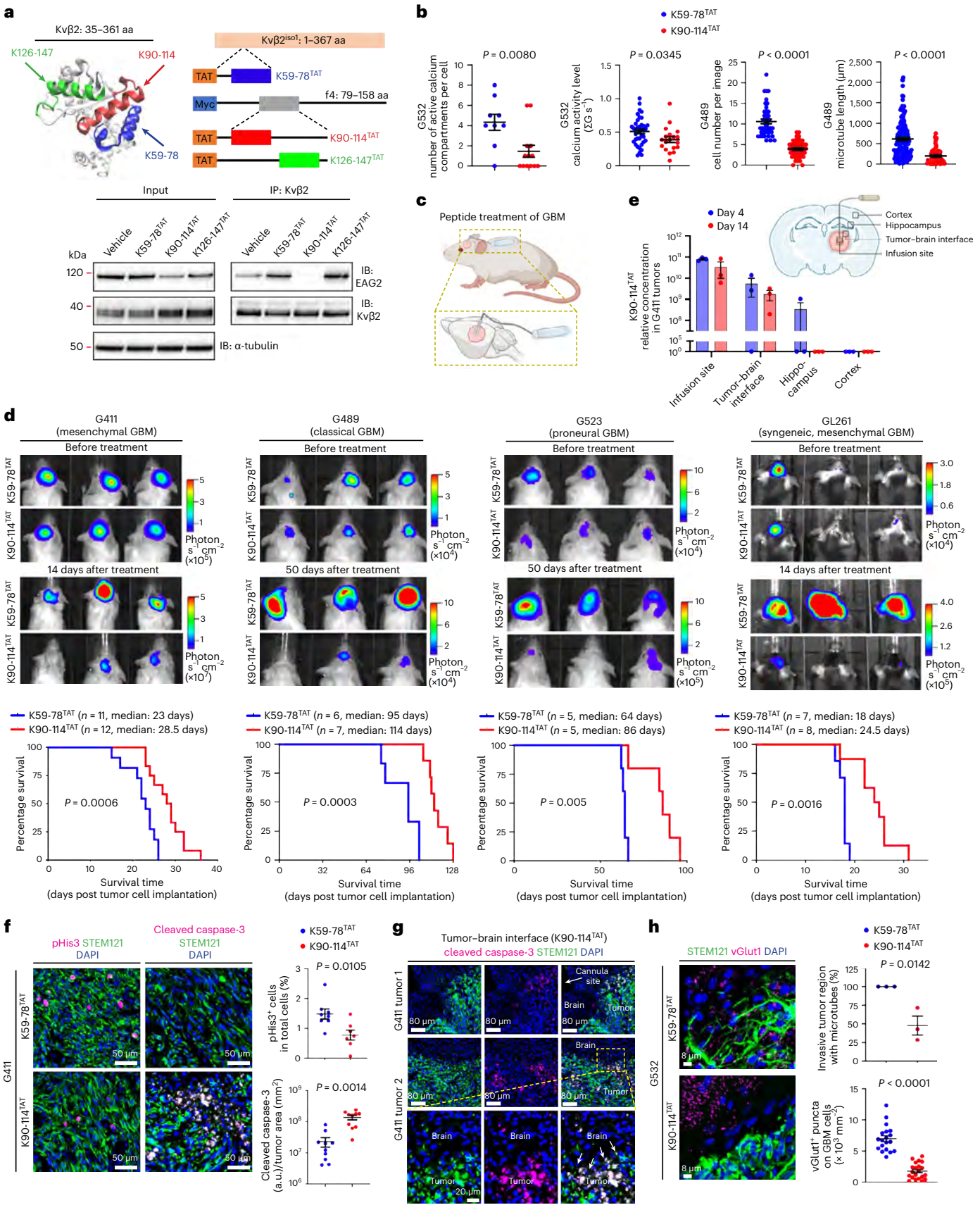

https://doi.org/10.1038/s43018-023-00626-8

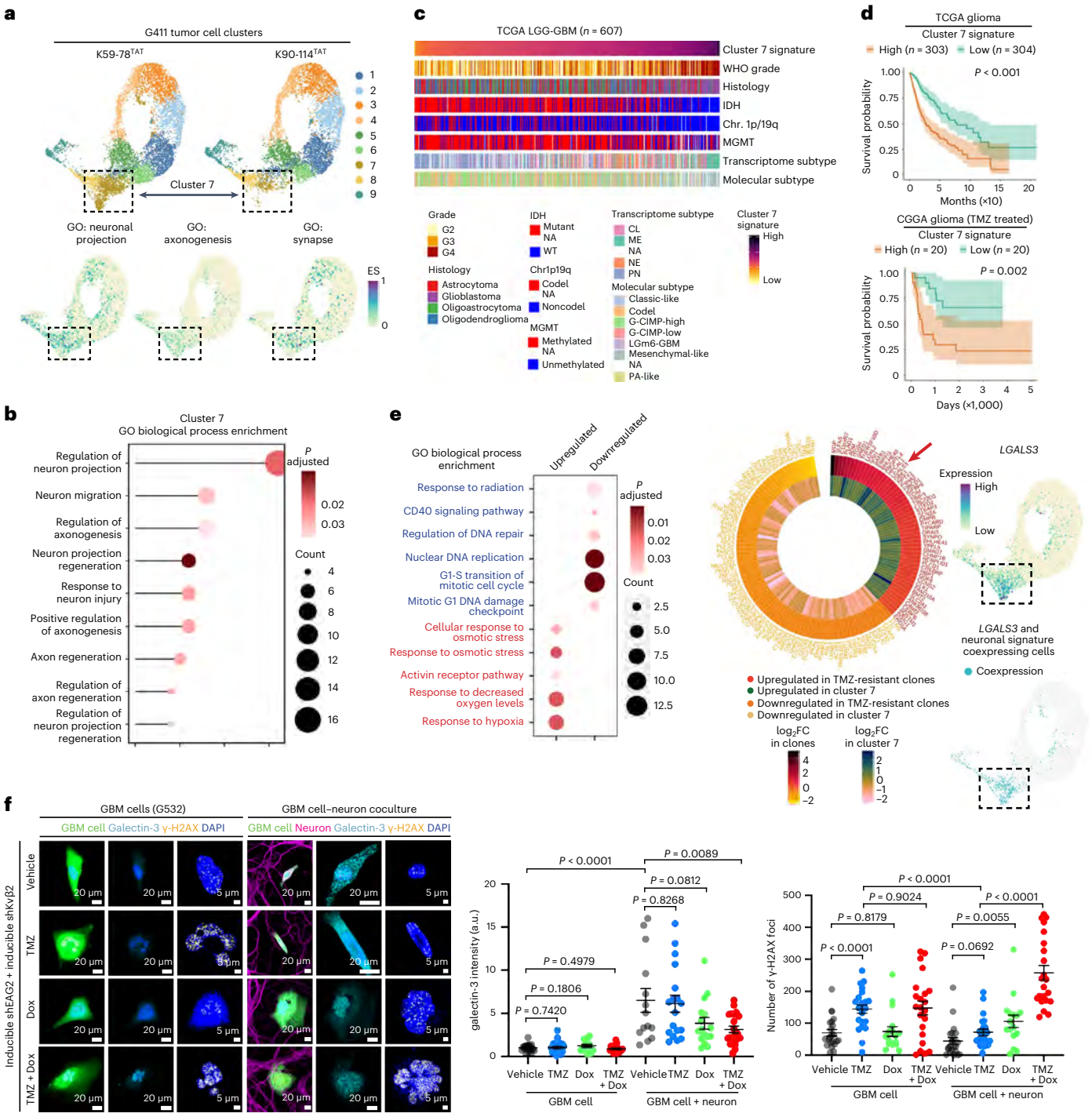

Fig. 6 | Cluster 7 GBM cells signify aggressive and TMZ-resistant GBM. a, Top, UMAP of scRNA-seq data showing nine GBM cell clusters. Bottom, GO biological pathway analysis of cluster 7 cells. ES, enrichment score. **b**, GO biological pathway enrichment analysis of cluster 7 cells. Adjusted *P* values, Benjamini–Hochberg method. **c**, Heatmap showing correlation between cluster 7 signature and glioma biomarkers. WT, wild type; codel: codeletion; IDHmut, IDH mutant; CL, classical; ME, mesenchymal; NE, neural; PN, proneural; NA, not applicable; G-CIMP, glioma CpG island methylator phenotype; PA-like, pilocytic astrocytoma-like. **d**, Correlation between cluster 7 signature and survival of patients with glioma. *P* values, log-rank test. Error bands, mean ± 1.96 s.e. **e**, Left, GO biological pathway enrichment analysis showing up- and downregulated signaling pathways in cluster 7 cells compared with other GBM tumor cell clusters shown in **a**. Adjusted *P* values, Benjamini–Hochberg method. Middle, genes simultaneously up- or downregulated in cluster 7 cells and TMZ-resistant clones are listed. Right, *LGALS3* expression in UMAP scRNA-seq data. **f**, Representative vehicle- and TMZ-treated GBM cells cultured with or without neurons. Graphs show quantification of LGALS3 intensity and γ-H2AX foci number under different conditions. Sample size (from left to right), *n* = 20, 26, 16, 17, 14, 18, 16, 21, 22, 22, 16, 22, 22, 22, 16, 22 cells examined over three independent experiments. *P* values, two-sided unpaired *t*-test. Error bars, mean ± s.e.m.

the activity of O^6-methylguanine methyltransferase (MGMT), which repairs O^6-methylation DNA damage induced by TMZ. Methylation of MGMT promoter suppresses MGMT expression, thereby increasing GBM cell TMZ sensitivity. In patients, high cluster 7 signature correlates with MGMT promoter demethylation (Fig. 6c), suggesting that cluster 7 tumor cells confer greater TMZ resistance. Indeed, higher cluster 7

https://doi.org/10.1038/s43018-023-00626-8

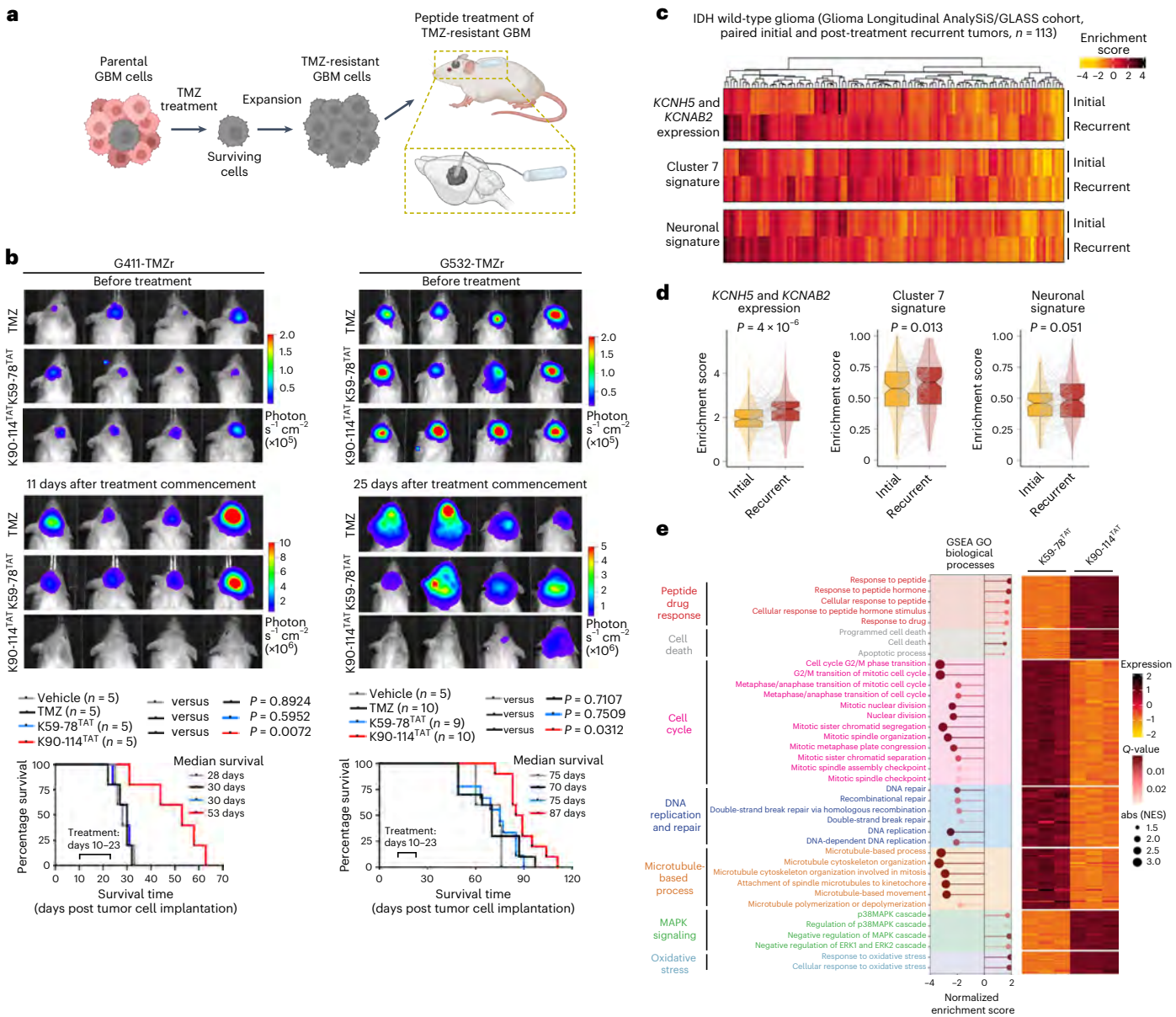

Fig. 7 | K90-114^{TAT} treatment is effective against TMZ-resistant GBM. **a**, Schematic showing the experimental procedure used to establish TMZ-resistant GBM cells, generate xenograft tumor and osmotic pump delivery of peptides. **b**, Bioluminescence images showing tumor burden before and after TMZ, K59-78^{TAT} or K90-114^{TAT} treatment. Kaplan–Meier survival curves of tumor-bearing mice are shown. *P* values, log-rank test. **c**, Heatmap showing *KCNH5* and *KCNAB2* expression, cluster 7 signature and neuronal signature in patient glioma tumors. Each column represents a paired initial–recurrent sample. **d**, Graphs showing the signature enrichment score of *KCNH5* and *KCNAB2* expression, cluster 7 signature and neuronal signature from **c**. *n* = 113 patients. *P* values were not adjusted and were calculated by two-sided paired Wilcoxon test. Box plot displaying 25th and 75th percentiles, with median represented by the center bar and whiskers showing 1.5× interquartile range. Outliers are represented by lines. Each line represents a paired initial–recurrent sample. **e**, RNA-seq showing transcriptomic response of GBM cells cocultured with neurons following K59-78^{TAT} or K90-114^{TAT} treatment. *n* = 3 biologically independent experiments. *Q*-value determined by false discovery rate (FDR). abs (NES), absolute (normalized enrichment score); GSEA, gene set enrichment analysis.

signature is strongly associated with worse survival in patients with glioma who received treatment with TMZ (Fig. 6d).

To acquire further insights into cluster 7 GBM cells, we compared cluster 7 genes with a published microarray dataset of patient-derived TMZ-resistant or -sensitive GBM cells[47] (Fig. 6e). We identified GO biological pathways shared between K90-114^{TAT}-targeted cluster 7 GBM cells and patient-derived TMZ-resistant GBM cells. Pathways that regulate DNA repair, cell cycle progression and response to radiation were downregulated in both cell types (Fig. 6e), consistent with the known roles of changes of these pathways in conferring chemoresistance. We identified a list of genes, including *LGALS3*, that are upregulated in both cluster 7 cells and patient-derived TMZ-resistant GBM cells (Fig. 6e). *LGALS3* encodes the carbohydrate-binding protein galectin-3, which promotes TMZ resistance and is associated with poor survival in patients with GBM[48]. Collectively, these data show that gene expression signature of K90-114^{TAT}-targeted cluster 7 GBM cells correlates with histological and molecular features of aggressive and TMZ-resistant gliomas.

K90-114^{TAT} effectively mitigates TMZ-resistant GBM

Because we found that K90-114^{TAT}-targeted cluster 7 GBM cells display both neuronal (Fig. 6a,b) and TMZ-resistant signatures (Fig. 6c–e),

https://doi.org/10.1038/s43018-023-00626-8

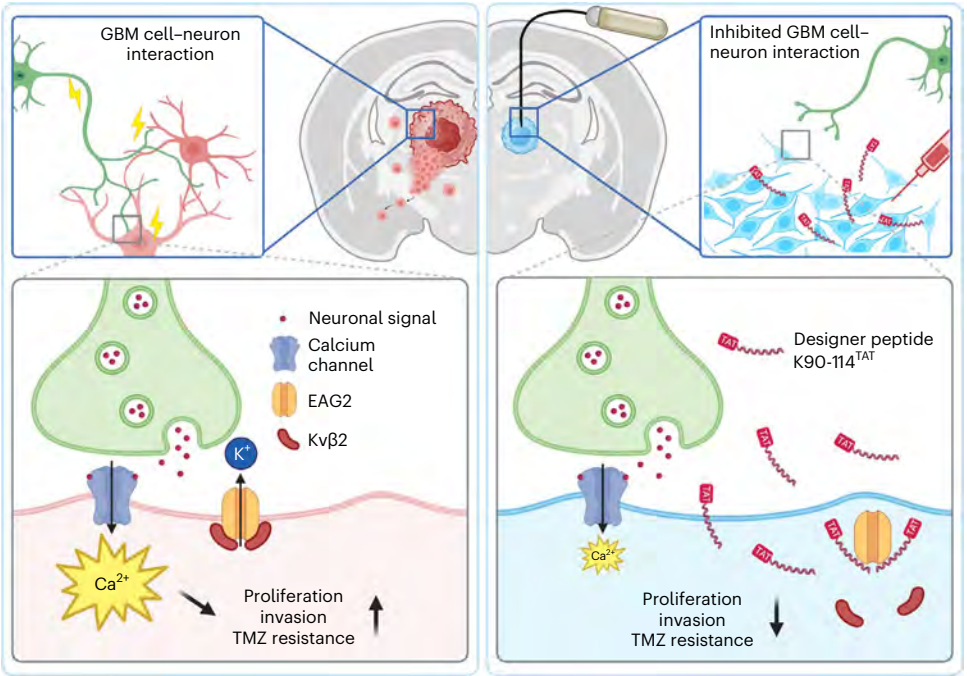

Fig. 8 | A designer peptide to treat GBM by disruption of EAG2–Kvβ2 potassium channel complex-mediated cancer–neuron interaction. EAG2 and Kvβ2 physically interact to form a potassium channel complex at neuron–GBM contact sites. The EAG2–Kvβ2 complex regulates Ca^{2+} transients of GBM cells and promotes GBM growth, invasion and chemoresistance. Designer peptide K90-114^{TAT} disrupts EAG2–Kvβ2 complex formation, mitigates GBM aggression and is efficacious in treating both TMZ-sensitive and -resistant GBM.

we investigated whether TMZ resistance of GBM cells depends on GBM cell–neuron interaction. Interestingly, *LGALS3* expression is not only highly enriched in cluster 7 GBM cells but is also associated with neuronal signature (Fig. 6e), suggesting that GBM cell–neuron interaction may upregulate TMZ-resistant genes such as *LGALS3* in GBM cells to promote TMZ resistance. To investigate this hypothesis, we studied vehicle- and TMZ-treated monocultured GBM cells or GBM cells cocultured with neurons, which revealed the following insights (Fig. 6f). First, neuron coculture elevated galectin-3 level in GBM cells. Second, neuron coculture decreased TMZ-induced DNA damage indicated by γ-H2AX foci number, revealing a role of GBM cell–neuron interaction in the promotion of TMZ resistance. Third, while combinatorial knockdown of EAG2 and Kvβ2 did not affect galectin-3 expression or TMZ resistance of monocultured GBM cells, it abrogated neuron-induced upregulation of galectin-3 and TMZ resistance of GBM cells. Together, these findings uncover a key role of EAG2 and Kvβ2 in mediation of neuron-dependent TMZ resistance of GBM cells.

Because TMZ is a cornerstone of GBM therapy, TMZ resistance underlies tumor recurrence and eventual treatment failure. To explore the therapeutic potential of K90-114^{TAT} for patients with TMZ-resistant (TMZr) GBM, we established TMZr cell lines[3] and performed orthotopic xenografts (Fig. 7a). G411-TMZr and G532-TMZr xenograft models were studied to determine the therapeutic efficacy of a 2-week peptide treatment regime on rapid- and slow-growing tumors, respectively. We started treatment after TMZr GBM tumors displayed substantial in vivo growth (10 days after xenograft). Treating mice with K90-114^{TAT}, but not with K59-78^{TAT} or TMZ, decreased tumor cell proliferation and increased tumor cell apoptosis (Extended Data Fig. 5), resulting in significantly reduced tumor burden and extension of mouse survival (Fig. 7b). In comparison with the marked therapeutic benefit seen in mice bearing G411-TMZr tumors, the modest yet significant benefit seen in K90-114^{TAT}-treated G532-TMZr models was probably due to the 2-week treatment period constituting a relatively shorter therapy administration window in the context of overall longer tumor growth and mouse survival time (Fig. 7b).

Post-standard therapy GBM recurrence is universally fatal. By comparison of matched initial and recurrent patient glioma tumors, a recent study by the Glioma Longitudinal AnalySiS (GLASS) Consortium reported that about 66% of IDH wild-type recurrent gliomas acquired a neuronal phenotype[30]. Importantly, these recurrent tumors with neuronal phenotype histologically mimic leading edge and infiltrating tumors defined by Ivy GAP[30]. Strikingly, we found that expression of *KCNH5* and *KCNAB2* is significantly upregulated in recurrent gliomas compared with matched initial tumors in patients (Fig. 7c,d). Furthermore, recurrent tumors showed elevated cluster 7 gene signature and neuronal signature (Fig. 7c,d). These findings provide further support the premise that EAG2 and Kvβ2 regulate GBM cell–neuron interaction, and highlight the therapeutic potential of designer peptide K90-114^{TAT} in the treatment of recurrent glioma by targeting tumor cells that are refractory to standard therapy.

To interrogate the potential mechanisms by which K90-114^{TAT} works, we treated the GBM cell–neuron coculture with K59-78^{TAT} or K90-114^{TAT} and performed RNA-seq. We distinguished transcripts of patient-derived GBM cells from mouse neurons, followed by bioinformatic analysis to identify altered signaling pathways in GBM cells (Fig. 7e). Remarkably, K90-114^{TAT} treatment activated transcriptomic responses identified as 'Response to peptide' and 'Response to drug'. K90-114^{TAT} treatment increased 'Cell death' transcriptomic signatures while decreasing pathways in 'Cell cycle', 'DNA repair' and 'Microtubule-based process'. These data strongly support our findings that K90-114^{TAT} acts as a peptide drug to induce GBM cell apoptosis (Fig. 5f,g and Extended Data Figs. 3 and 5), decrease GBM cell proliferation (Fig. 5f and Extended Data Figs. 3 and 5), hinder DNA repair (Fig. 6f) and inhibit GBM cell microtube formation (Figs. 3e and 5h)[49]. Furthermore, K90-114^{TAT} treatment activated transcriptomic response conducive to activation of p38 MAPK signaling, suppression of ERK1/2-dependent signaling and cellular response to oxidative stress. While we previously showed that EAG2 deficiency activates p38 MAPK signaling to suppress tumor growth in medulloblastoma[50], the engagement of ERK1/2 and oxidative stress signaling provides direction for future study.

Discussion

Glioblastoma is the most common and deadly primary brain cancer. To date, identifying disease vulnerability with GBM-specific mechanism of action and developing therapeutic approaches to target such a mechanism are key to treating this 'untreatable disease'. Recent studies have uncovered multifaceted roles of the nervous system in regulating malignant behaviors of central nervous system tumors[6,9,10,13,14], brain metastases[16] and tumors outside the central nervous system[8,12]. The discovery of crosstalk between tumor cells and neurons has initiated the field of 'cancer neuroscience', an apt term that highlights the importance of elucidating tumor–neuron interactions to uncover therapeutic opportunities[51]. Potential therapeutic avenues include suppression of neuron hyperexcitation, inhibition of GBM cell–neuron synapse formation, perturbation of synaptic transmission, blocking of neuron activity-induced downstream signaling and blocking of tumor network transmission[52]. However, because cancer cells frequently hijack the cellular and molecular mechanisms of normal neurophysiological processes to propel their malignant behaviors, identifying a molecular 'weakness' unique to tumors is highly desired but thus far unachieved.

In this study we report that potassium channel EAG2 and its auxiliary subunit Kvβ2 physically interact to form a complex. EAG2 displays Kvβ2-dependent localization at GBM cell–neuron contact sites. Genetic knockdown of EAG2 and Kvβ2 dampens calcium transients of GBM cells, decreases GBM cell proliferation and invasion and prolongs the survival of tumor-bearing mice. We discovered that Kvβ2 isoform 4, which is uniquely expressed in GBM cells at high levels, mediates EAG2–Kvβ2 complex formation. Therefore, EAG2–Kvβ2 protein–protein interaction (rather than EAG2 or Kvβ2 separately) represents a GBM-specific disease vulnerability. Our identification of Kvβ2 amino acids 79–158, which mediate EAG2–Kvβ2 interaction, led to the rational design of multiple TAT-conjugated, cell-penetrable peptides. Among these peptides, K90-114^{TAT} disrupts EAG2–Kvβ2 interaction. In agreement, K90-114^{TAT} possesses robust efficacy in treating TMZ-sensitive and -resistant GBM, with no signs of toxicity detected in nontumoral tissues. We previously showed that EAG2 regulates premitotic cytoplasmic condensation, a cell volume reduction process required for mitotic entry, to promote medulloblastoma growth[50]. We showed that EAG2 enriches to the trailing edge of medulloblastoma cells to promote cell rear retraction, tumor cell motility and medulloblastoma metastasis[53]. More recently we showed that chloride channel CLIC1 and EAG2 coregulate the efflux of chloride and potassium, which is required for the rapid division of tumor cells in medulloblastoma[54]. Herein we identified EAG2–Kvβ2 protein–protein interaction as a GBM target, elucidated its mechanism of action and developed a designer peptide for functional interference and therapeutic treatment (Fig. 8). Our continuous studies of EAG2 constitute the literature that reports the roles of EAG2 in brain cancer.

Although we uncovered the roles of the potassium channel in regulation of GBM cell–neuron interaction and engineered an approach to treat GBM, our findings provide strong impetus to investigate the following questions. First, K90-114^{TAT}-targeted cluster 7 GBM cells exhibit gene signatures in both neuronal projection and TMZ resistance, revealing a connection between GBM cell–neuron interaction and chemoresistance. We discovered a list of upregulated genes shared between cluster 7 GBM cells and patient-derived TMZ-resistant GBM cells. Within this list, multiple genes, including *MGP*[55], *ADM*[56] and *LGALS3* (ref. 48), have been associated with TMZ resistance. Functional interrogation of cluster 7-enriched genes will offer insights into tumor–neuron interaction and neuron-dependent therapy resistance of GBM. Second, glioma microtubes interconnect tumor cells to form a proliferative, invasive and therapy-resistant network[19,31]. Targeting tumor microtubes represents a key approach to treat glioma[52]. Because we found that genetic knockdown of EAG2 and Kvβ2 and K90-114^{TAT} treatment robustly suppressed GBM microtube formation, uncovering the signaling regulated by EAG2 and Kvβ2 should illuminate the mechanistic basis underlying the microtube-based glioma cellular network. Third, 'microsatellites' infiltrating tumor cells, which are not fully resectable, function as 'seeds' of GBM recurrence. The fact that EAG2 and Kvβ2 are prominently expressed at the tumor–brain interface and in recurrent patient tumors highlights the potential of our designer peptide K90-114^{TAT} in treatment of glioma recurrence. Future preclinical research and clinical trials should include recurrent glioma in the study design. Fourth, while this work focuses on GBM–neuron interaction, whether EAG2 and Kvβ2 regulate GBM cell–astrocyte interaction and GBM cell-intrinsic properties warrants future investigation.

We used osmotic pumps and cannula guidance to deliver designer peptide K90-114^{TAT} into GBM. While this delivery method is principally similar to Ommaya Reservoir, a local delivery method used in clinics, we envision additional delivery routes. Nerinetide, which recently completed phase III trials in the treatment of acute ischemic stroke, is composed of the TAT-conjugated C terminus of NR2B9c, a nine-amino-acid residue inhibitor of the interaction between NMDA receptors and PSD95. Because TAT is engineered to deliver intravenously administered nerinetide across the blood–brain barrier[57,58], it would be informative to determine the pharmacokinetics, pharmacodynamics, potency and potential side effects of peripherally administered K90-114^{TAT} in treatment of GBM. Wafer-mediated slow release of a chemotherapeutic agent, such as carmustine (brand name Gliadel), is used to treat patients with GBM by placing a drug-containing wafer in the cavity following surgical tumor resection. Wafer-mediated slow release of K90-114^{TAT} at the tumor resection site can also be considered in the treatment of GBM. Both ion channels and protein–protein interactions require modulation of a large surface area within the proteins to induce a therapeutic response. We developed designer peptide K90-114^{TAT}, which features marked tumor selectivity and minimal nontumoral toxicity, to target cancer–neuron interaction. Optimizations in peptide delivery methods and dosing schemes, as well as development of combination therapy (based on peptide impact on tumor–astrocyte interaction, tumor cell-intrinsic properties, the immune microenvironment and so on) are important future directions. We envision that this designer peptide will be developed into a therapeutic modality to benefit patients with GBM.

Methods

Cell lines

Patient-derived GBM cells (G411, G489, G508, G523, G532, G583, G620, G691r, G799 and G800) and human fetal neural stem cells (hf6562 and hf7450) are generated in the Peter Dirks laboratory at the Hospital for Sick Children. GL261 cells are from the Justin Lathia laboratory at the Cleveland Clinic. HEK293T cells and human astrocytes are from the James Ellis laboratory at the Hospital for Sick Children. Lung cancer cells (PC9 and H1975) are from the Shana O. Kelley laboratory at the University of Toronto. Chinese hamster ovary (CHO) cells were purchased from Sigma-Aldrich (no. 85051005-1VL).

Patient-derived GBM cells and human fetal neuron stem cells were cultured using Neurocult NS-A basal medium (human, Stemcell Technologies) supplemented with 2 mM L-glutamine, 1× B27 without vitamin A (Gibco), 1× hormone mix (in-house N2 supplement), 75 μg ml^{-1} bovine serum albumin, 20 ng ml^{-1} human recombinant human epidermal growth factor and basic fibroblast growth factor (Stemcell Technologies) and 2 μg ml^{-1} heparin (Sigma-Aldrich). Half of the medium was replaced with fresh every 3 days. PC9 and H1975 cells were cultured in RPMI medium with 10% fetal bovine serum (FBS). GL261, HEK293T and CHO cells were cultured using DMEM medium with 10% FBS. Human astrocytes were cultured in complete Astrocyte Medium (ScienCell, no. 1801). All cell lines are tested as being negative for mycoplasma.

Transfection and lentivirus production

For immunoblotting and co-IP, 1 μg of EAG2 plasmid and 0.5–4.0 μg of Kvβ2 isoform 1–5 plasmids were transfected into HEK293T cells cultured in 60-mm dishes using PolyEZ (BioMart) and incubated for 24 h. For lentivirus production, 15 μg of lentiviral vectors, 10 μg of Gag-pol,

Rev and Tat vectors and 5 µg of VSV-G vectors were transfected into HEK293T cells cultured in T75 flasks. Eight hours after transfection, media were replaced with DMEM medium containing 10% FBS and 1× NEAA (ThermoFisher). Forty-eight hours later, virus-containing medium was collected and centrifuged at 4 °C for 2 h at 25,000 rpm (average 82,705*g*, maximum 112,700*g*, *k*-factor 308). Viral pellets were dissolved in ice-cold Dulbecco's PBS (DPBS), aliquoted and stored at −80 °C.

Generation of stable cell lines

GBM cells were transduced with Dox-inducible short-hairpin RNA lentiviruses and selected for positive cells with 1 µg ml^{-1} puromycin. Cells were transduced again with either green fluorescent protein (GFP) lentivirus (Addgene, no. 22479), luciferase-GFP lentivirus (Addgene, no. 80389) or GCaMP6s-tdTomato lentivirus (Addgene, no. 80316) and sorted for GFP- or tdTomato-positive cells using fluorescence-activated cell sorting.

Generation of TMZ-resistant cell lines

TMZ (Sigma, no. T2577-100MG) was dissolved in DMSO to a stock concentration of 100 mM and further diluted in complete NS-A medium to concentrations of 10, 20, 50, 100, 200 and 400 µM. For each concentration, GBM cells were seeded at 30% confluency and cultured until confluent before being subjected to higher TMZ concentrations. Once TMZ-resistant cell lines were established, cells were cultured constantly under 200 µM TMZ to maintain their resistance.

GBM cell–neuron and GBM cell–astrocyte coculture

Primary mouse neurons and astrocytes were extracted from E18.5 wild-type mouse embryos using the Papain dissociation system (Worthington, no. LK003150). Cells (8.5×10^4) were seeded onto 12-mm coverslips coated with poly-L-ornithine (Sigma-Aldrich, no. P4957) and laminin (Simga-Aldrich, no. L2020-1MG). Neurons, astrocytes and cocultured GBM cells were cultured in Neurobasal Plus medium (ThermoFisher) supplemented with 1× B27 Plus (ThermoFisher) and 0.5 mM GlutaMax (ThermoFisher). These were maintained in medium for 4 days and then fed every 3 days by removal of half of the medium and replenishment with fresh. For neuron culture, 1 µg ml^{-1} 5-fluoro-2′-deoxyuridine (FUDR, Sigma-Aldrich) was added once at days in vitro (DIV) 1 to suppress astrocyte growth. For astrocyte culture, neurons were killed by exposure to air for several seconds by complete removal of culture medium. For the GBM cell–neuron coculture experiment, GBM cells with Dox-inducible shRNAs were pretreated with 1 µg ml^{-1} Dox or vehicle for 4 days; Dox concentration was consistent during coculture. For calcium imaging, 5,000 GCaMP6s$^+$; tdTomato$^+$ GBM cells were seeded into neuron culture at DIV 13 and cocultured for 1–3 days. For the GBM proliferation and tumor microtube assays, 5,000 GFP$^+$ GBM cells were seeded with or without neurons (DIV 14–21) and cocultured for 4 days. For TMZ treatment, 2,000 GFP$^+$ GBM cells were cocultured with neurons (DIV 14–21) for 3 days before treatment with 200 µM TMZ or vehicle for a further 3 days.

Peptide sequence, reconstitution, storage and in vitro treatment

All peptides were purchased from GL Biochem, with purity >95%. Peptides were reconstituted with DPBS to a stock concentration of 50 mg ml^{-1} (molarities were calculated), aliquoted, snap-frozen using liquid nitrogen and stored at −80 °C. For in vitro EAG2–Kvβ2 co-IP with peptide treatment, G532 and G411 cells were cultured in 60-mm dishes until confluent, treated with 50 µM K59-78^{TAT}, K90-114^{TAT}, TAT, K90-114 or K126-147^{TAT} for 4 h and washed three times with DPBS before protein extraction. For calcium imaging with peptide treatment, 20 µM K59-78^{TAT} or K90-114^{TAT} was added to GBM cell–neuron cocultures 16 h before imaging. For the GBM cell number and microtube experiment with peptide treatment, GBM cells were pretreated with 50 µM K59-78^{TAT} or K90-114^{TAT} for 16 h and then the same number of GBM cells was seeded into DIV 10–13 neurons and cocultured for 3 days. Peptide sequences are listed in Supplementary Table 1.

Immunoblotting and co-IP

Total proteins were extracted using lysis buffer containing 50 mM HEPES, 150 mM NaCl, 10% glycerol, 1 mM EDTA, 1% NP-40, 1× protease inhibitors cocktail (Pierce, no. A32955) and 1 mM dithiothreitol (DTT). All steps were carried out at 4 °C. Protein concentrations were measured using colorimetric assay (Bio-Rad). For co-IP, lysates were incubated with 1 µg of either normal IgG or bait antibody overnight. Next, 40 µl of Protein G resin (GE healthcare) was added to the lysates with incubation for a further 2 h and washing four times with lysis buffer. Co-IP samples were collected by the addition of 20 µl of 2× lithium dodecyl sulfate (LDS) sample buffer (Invitrogen) containing 50 mM DTT to resins and heating at 70 °C for 10 min. Protein samples (10 µl for co-IP or 10 µg for immunoblotting) were resolved on 10% Bis-Tris gel (Invitrogen) at 200 V with MES running buffer (Invitrogen). Proteins were then transferred to polyvinylidene difluoride membrane (Millipore) and blocked with either 5% bovine serum albumin (Sigma) or nonfat milk (Bio Basic) and 0.1% Tween-20 in Tris buffered saline. Immunoblot assays were performed using primary antibodies diluted in the blocking solution. Immunoreactive bands were visualized using the Bio-Rad Chemidoc imaging system. The antibodies used for co-IP were rabbit anti-EAG2 (Alomone labs, no. APC-053), mouse anti-Kvβ2 (Millipore, no. MABN652) and mouse anti-Myc (Santa Cruz Biotechnology, no. sc-40). The primary antibodies for immunoblotting were rabbit anti-EAG2 (Alomone labs, no. APC-053, 1:2,000), mouse anti-EAG2 (Santa Cruz Biotechnology, no. sc-398458, 1:200), mouse anti-Kvβ2 (Millipore, no. MABN652, 1:2,000), mouse anti-Myc (Santa Cruz Biotechnology, no. sc-40, 1:1,000), rabbit anti-Myc (Santa Cruz Biotechnology, no. sc-789, 1:1,000) and mouse anti-α-tubulin (Sigma-Aldrich, no. T6199, 1:5,000). Secondary antibodies were goat anti-rabbit IgG HRP conjugated (Cell Signaling Technology, no. 7074P2,1:10,000) and goat anti-mouse IgG HRP conjugated (Cell Signaling Technology, no. 7076P2, 1:10,000).

Mice and housing conditions

NOD scid gamma (NSG, no. J#5557) mice and C57BL/6 J (BL6) mice used in this study were kept in a sterile environment under a 12/12-h light/dark cycle, 21–23 °C and 40–60% humidity at The Centre for Phenogenomics in Toronto, Canada.

In vivo experiments

In total, 2,000 G411 or G411-TMZr cells and 1×10^5 G532-TMZr, G489 or G523 cells were orthotopically injected into 6–12-week-old female NSG mice; GL261 cells (10,000) were orthotopically injected into 6–12-week-old female BL6 mice. The coordinates were 1.5 mm lateral to midline, 2 mm posterior to bregma and −3 mm deep to the cranial surface. Mice were given a 10-day recovery period unless specified otherwise. On day 10, BLI was used to assess tumor growth. Mice with comparable tumor sizes were randomly allocated to each experimental group. BLI was performed using the Xenogen IVIS Lumina System with Living Image software for data collection. For Dox-inducible knockdown, one group of mice received Dox-containing food (625 mg kg^{-1}, ENVIGO) while the other received regular food. In the case of peptide treatment, preassembled osmotic pumps (Alzet, model no. 1002 #0004317) loaded with peptides were immersed in DPBS and incubated overnight at 37 °C. The daily peptide infusion rate was 300 µg unless stated otherwise. The peptide treatment shown in Extended Data Fig. 2d was done at day 4 post xenograft with the osmotic pump model (Alzet, model no. 1007D #0000290). For TMZ treatment, TMZ (Sigma, no. T2577-100MG) was dissolved in Kolliphor EL (Sigma, no. C5135-500G) to 5 mg 100 µl^{-1} (10× stock, stored at 4 °C) and further diluted to 1× with

distilled water; 25 mg kg^{-1} TMZ was then gavage fed for five consecutive days from day 10 post xenograft.

Immunofluorescence staining

Cultured cells. Cells on coverslips were fixed using ice-cold 4% paraformaldehyde for 20 min and permeabilized with 0.3% Triton-X in DPBS (with Ca^{2+} and Mg^{2+}, Sigma-Aldrich) for 5 min. Cells were then blocked with 10% normal goat serum (Gibco) in DPBS for 1 h and incubated with primary antibodies at 4 °C overnight and secondary antibodies for 2 h at room temperature. After each procedure, a total of three washes with DPBS were performed. Coverslips were mounted with ProLong diamond Antifade Mountant (Invitrogen, no. P3696). All antibodies were diluted in blocking buffer. The primary antibodies used were chicken anti-TUJ1 (Aveslabs, no. TUJ1, 1:1,000), rabbit anti-EAG2 (Alomone labs, no. APC-053, 1:1,000), mouse anti-PSD95 (Invitrogen, no. Ma1-046, 1:500), mouse anti-LGALS3 (Santa Cruz Biotechnology, no. sc-32790, 1:500) and rabbit anti-γH2AX (Cell Signaling Technology, no. 2577S, 1:1,000).

Tumor sections. Tumor-bearing mice were perfused with PBS and 4% paraformaldehyde. Brains were sectioned at a thickness of 10 µm. Tumor sections were permeabilized with 0.3% Triton-X in PBS for 10 min and incubated with blocking buffer (10% normal goat serum, 0.1% Tween-20 in PBS) for 1 h, followed by incubation with primary antibodies at 4 °C overnight and secondary antibodies for 2 h at room temperature. After each precedure, a total of three washes with PBST (0.1% Tween-20 in PBS) were performed. Primary antibodies were rabbit anti-EAG2 (Alomone labs, no. APC-053, 1:300), rabbit anti-Kvβ2 (Alomone labs, no. APC-117, 1:300), mouse anti-Kvβ2 (Santa Cruz Biotechnology, no. sc-393014, 1:200), mouse anti-Tau (Santa Cruz Biotechnology, no. sc-32274, 1:200), chicken anti-GFAP (Millipore, no. AB5541, 1:300), guinea pig anti-vGlut1 (Millipore, no. AB5905, 1:1,000), mouse anti-STEM121 (TaKaRa, no. Y40410, 1:500), rabbit anti-pHis3 (abcam, no. ab5176, 1:500) and rabbit anti-cleaved Caspase-3 (Cell Signaling Technology, no. 9661, 1:500).

Secondary antibodies used for immunofluorescence staining were goat anti-chicken Alexa 405 conjugated (1:500, abcam, no. ab175674), goat anti-chicken Alexa 488 conjugated (1:500, abcam, no. ab150169), donkey anti-mouse Alexa 488 conjugated (1:500, Jackson ImmunoResearch, no. 715-546-151), goat anti-mouse Alexa 532 conjugated (1:500, ThermoFisher, no. A-11002), goat anti-rabbit Alexa 555 conjugated (1:500, ThermoFisher, no. A-21428), donkey anti-guinea pig Alexa 594 conjugated (1:500, Jackson ImmunoResearch, no. 706-585-148) and donkey anti-rabbit Alexa 647 conjugated (1:500, Jackson ImmunoResearch, no. 711-605-152).

Cloning and plasmid information

EAG2 and Kvβ2 isoform 5 vectors were purchased from Horizon (nos. MHS6278-202760120 and MHS6278-202801524); Kvβ2 isoform 1 was cloned from complementary DNA of a GBM stem cell line using primer pair f1 forward and f3 reverse (listed in Supplementary Table 1) and cloned into the pCMV-Myc (Clontech, no. K6003-1) mammalian expression system via EcoRI and XhoI. The Kvβ2 isoform 3-Myc mammalian expression vector was purchased from Origene (no. RC232680). Kvβ2 isoform 2 and 4 vectors were generated from the pCMV-Myc-Kvβ2 isoform 1 plasmid using the primer pairs listed in Supplementary Table 1. Kvβ2 fragments were generated using the primer pairs listed in Supplementary Table 1. f1, f2 and f3 were generated using their corresponding primer pairs, f4 was generated using f2 forward and f1 reverse, f5 was generated using f3 forward and f2 reverse and f6 was generated using f6 forward and f3 reverse.

For Dox-inducible shRNA vectors, the pLKO-Tet-On backbone was purchased from Addgene (no. 21915); shRNA oligos were synthesized and cloned into the backbone via AgeI and EcoRI. shRNA sequences are listed in Supplementary Table 1.

qPCR for Kvβ2 isoform 4

Total RNAs for each cell line were extracted using the GENzol TriRNA pure Kit (Geneaid): 1 µg of total RNA was reverse transcribed into cDNA using the sensiFAST cDNA synthesis kit (Bioline). EmeraldAmp Max PCR Master Mix (TaKaRa, no. RR320A) was used, and bands at 186 bp were quantified using Image Lab software (Bio-Rad). Quantitative PCR (qPCR) primers for Kvβ2 isoform 4 and GAPDH are listed in Supplementary Table 1.

Quantification of immunofluorescence images

Infiltrating tumor colony number, infiltrating tumor/tumor core ratio, tumor area, tumor boundary sinuosity and tumor boundary type. Tumor sections were scanned with a 3DHistech Slide Scanner using the ×40/0.95 numerical aperture objective. Tumor sections were viewed and analyzed using SlideViewer software. STEM121 was used to mark tumor. Both infiltrating tumor colony and tumor core were manually marked. Only those tumor colonies of area >100,000 $µm^2$ were counted. Tumor boundary length was marked manually. Tumor boundary sinuosity was measured using boundary length divided by distance. Tumor boundary types were determined manually based on definitions.

vGlut1 and γH2AX puncta, microtube length and number, EAG2, Kvβ2, cleaved caspase-3 and galectin-3 mean intensity and pHis3 percentage. Tumor sections and cocultured cells were imaged using a Leica SP8/STED microscope and quantified with Imaris software. vGlut1 and γH2AX puncta were quantified using spot function. Tumor-associated vGlut1 puncta were defined as spots located within STEM121 regions. γH2AX puncta were defined as signals within each nucleus. Microtube length and number were quantified using filament function. EAG2, Kvβ2, cleaved caspase-3 and galectin-3 intensity were quantified using surface function. Signals within STEM121 and GFP were collected, and mean intensity was calculated by dividing total intensity by the area of STEM121 or GFP. pHis3 was quantified using cell function, and percentage was calculated by dividing $pHis3^+$ cells by total $DAPI^+$ cells.

GBM cell number. Nine images were taken in a 3 × 3 cubic manner from each individual slide, and the number of GBM cells in each image was quantified manually using ImageJ with the cell counter add-on.

G489 and GL261 tumor quantification. Tumors were imaged using a 3DHistech Slide Scanner, and $pHis3^+$, cleaved $caspase\text{-}3^+$ and total GBM cell number were quantified using QuantCenter and PannoramicViewer. Briefly, a cell quant was created in QuantCenter for each slide. The threshold was carefully adjusted to separate positive and negative signals. Six regions in each tumor section were manually selected. $pHis3^+$ and cleaved $caspase\text{-}3^+$ cells were collectively quantified in PannoramicViewer using the threshold defined in the previous steps.

Calcium imaging

$GCaMP6s^+$; $tdTomato^+$ G532 cell–neuron cocultures were transferred to the imaging chamber with continuous perfusion (~2 ml min^{-1}) at room temperature (22 °C) with extracellular medium containing 140 mM NaCl, 2.5 mM KCl, 10 mM HEPES, 33 mM glucose and 1.3 mM $CaCl_2$; pH was adjusted to 7.3 with NaOH. The GBM cells were visualized on an upright microscope (Axio Examiner, Carl Zeiss) equipped with a charge-coupled device monochrome video camera (IR-1000, DAGE-MTI) and identified by their shape, size and tdTomato fluorescence. Tumor cells with dense neural connectivity and healthy morphology were chosen for time-lapse, live-cell imaging. Images were acquired by a confocal laser scanning microscope (LSM 710 NLO, Carl Zeiss) at ~2 Hz frame rate through a ×63 water-immersion objective (1.0 numerical aperture, W Plan-Apochromat, Carl Zeiss). First, we reconstructed the three-dimensional morphology of tumor cells by tdTomato fluorescence. Next, we followed the spontaneous Ca^{2+}

activity of tumor cells for 12.5 min by imaging GCaMP6s fluorescence with a 488-nm argon laser. Active compartments in each GBM cell were defined manually based on visual identification of green fluorescence fluctuations. Each active compartment of the tumor cell is defined by spontaneous and localized Ca^{2+} transients unique to that compartment. The Ca^{2+} level in each active compartment was defined according to the following equation:

$$G/R = \frac{G_{Ac} - G_{Bg}}{R_{Ac} - R_{Bg}}$$

where G and R are the mean fluorescence intensity of GCaMP6s and tdTomato signals, respectively, at active compartments (Ac) or in the background (Bg), defined as an area devoid of tumor cells. The Ca^{2+} level per second was defined as the area under the curve throughout the entire experiment normalized to 1 s. Zen, Excel and Igor Pro 6.0 software were used to analyze data. Calcium traces from each active compartment were imported into GraphPad Prism to generate heatmaps.

Patch clamp recording

Chinese hamster ovary cells were plated on coverslips and transfected with 0.5 µg of EAG2 cDNA with either 1.5 µg of Kvβ2 isoform 4 cDNA or an equal amount of empty vector. Patch clamp recordings were performed 24–48 h post transfection. Coverslips were placed in a recording chamber filled with bath solution consisting of 118 mM NaCl, 3 mM KCl, 2.5 mM $CaCl_2$, 1.5 mM $MgCl_2$, 10 mM glucose and 10 mM HEPES; pH was adjusted to 7.4 with NaOH. Patch pipettes (borosilicate glass), with resistance of around 4 MΩ, were filled with intracellular solution containing 125 mM KCl, 11 mM EGTA, 1 mM $CaCl_2$, 1.5 mM $MgCl_2$ and 10 mM HEPES; pH was adjusted to 7.2 with KOH. Whole-cell currents were recorded using an Axopatch 700B amplifier (Molecular Devices) at room temperature, and both pipette and whole-cell capacitance were compensated. The voltage protocol consisted of 200-ms pulses ranging from −80 to +80 mV (in 20-mV voltage steps). Data were acquired online, filtered at 4 kHz, digitized at 10 kHz and analyzed offline using pClamp10 (Molecular Devices). Leak currents before voltage stimulations were subtracted offline. I–V curves were generated by plotting peak current amplitude at different voltages.

Mass spectrometry

Tissue collection. G411 GBM-bearing, K90-114^{TAT} pump-implanted mice were prepared as described above. At days 4 and 14 post pump implantation, mice were humanely killed by cervical dislocation and brains immediately dissected and placed on ice. Brains were cut in half at the injection site using a scalpel, and tissues from the injection site, tumor–brain interface, hippocampus and cortex were carefully dissected, snap-frozen in liquid nitrogen and stored at −80 °C.

Brain samples. Frozen tissue samples were manually homogenized and diluted in TONG Lysis buffer with 10 mM tris(2-carboxyethyl)phosphine and 3.7 mg ml^{-1} chloroacetamide. Samples were sonicated for 15 s at 4 W and protein was extracted using chloroform/methanol. Proteins were subjected to mass spectrometry analysis as described below.

K90-114^{TAT} identification. Approximately 23 µg of K90-114^{TAT} was diluted in 50 mM ammonium bicarbonate and reduced with 10 mM DTT for 1 h at 60 °C, and alkylated in 20 mM iodoacetamide for 45 min at room temperature in the dark. Peptide was digested in trypsin (Pierce) at 37 °C overnight. Samples were desalted in C18 ZipTips (Millipore), lyophilized and resuspended in 2% ACN and 0.1% formic acid then separated on a 75 µm × 50 cm PepMap RSLC EASY-Spray column filled with 2 µM C18 beads (ThermoFisher). Data were collected on an Orbitrap Fusion Lumos mass spectrometer connected to an EASY-nanoLC 1200 system (Thermo Scientific). The liquid chromatography portion of the analysis consisted of an 18-min linear gradient running from 3 to 20% buffer B (80% acetonitrile and 0.1% formic acid), followed by a 31-min linear gradient running from 20 to 35% buffer B and a 2-min ramp to 100% buffer B, which was held for an additional 9 min. Mass spectrometry 1 acquisition resolution was set to 120,000, with an automatic gain control target value of 4×10^5 and maximum injection time of 50 ms over a scan range of 375–1,500 m/z. Peptides with a charge state between 2 and 7 above a global intensity threshold of 10,000 were collected with a dynamic exclusion set to 10 s. Isolation for mass spectrometry 2 scans was performed in the quadrupole with an isolation window of 0.7 m/z. Mass spectrometry 2 scans were performed in the ion trap with a maximum injection time of 10 ms, automatic gain control target value of 1×10^4 and higher-energy collisional dissociation activation with a normalized collision energy of 30 (ThermoScientific). Data were analyzed using PEAKS Studio 10.6 build 20201221. All mass spectrometry experiments were performed by SPARC BioCentre Molecular Analysis, The Hospital for Sick Children, Toronto, Canada.

Data analysis. Mass spectrometry raw files were analyzed using Proteome Discoverer (v.2.5.0.400) and fragment lists searched against a modified mouse UniProt Reference database (Uniprot_UP000000589, downloaded 15 September 2020). Both mass spectroscopy Amanda and Sequest HT were used as search algorithms, with parent and fragment mass tolerances set to 50 ppm and 0.6 Da, respectively. Three missed tryptic cleavages were allowed and carbamidomethylation of cysteine was specified as a fixed modification, with deamidation of asparagine and glutamine, oxidation of methionine and acetylation of the protein N terminus specified as variable modifications.

Bioinformatics

RNA extraction from GBM cell–neuron coculture for RNA-seq. In total, 10,000 G411 cells were seeded into DIV 7 neuron cultures and cocultured for 3 days; 50 µM of K59-78^{TAT} or K90-114^{TAT} was added to cultures with incubation for 8 h. Total RNA was extracted from treated cells using the RNeasy Mini Kit (Qiagen). Sample quality control, library preparation and sequencing were performed by The Center for Applied Genomics, The Hospital for Sick Children, Toronto, Canada.

Tumor–neuron coculture RNA-seq analysis. Raw sequencing data from above were mapped to mm10 and hg38 reference genomes, respectively, using the HISAT2 toolkit (v.2.2.1). The R package XenofilteR (v.1.6) was applied to exclude RNA sequence reads from mouse neurons and to obtain human-specific GBM cell transcripts. The R package DESeq2 (v.1.32.0) was used to detect differentially expressed genes between K90-114^{TAT}- and K59-78^{TAT}-treated cells. Differentially expressed genes with FDR < 0.05 and $|\log_2(\text{fold change (FC)})| > 0.5$ were accepted as significant. These genes were sorted by $\log_2$(FC) as input to the gene set enrichment analysis algorithm in the R package clusterProfiler for Gene Ontology (GO) enrichment analysis. NES > 0 indicates upregulated biological processes in K90-114^{TAT}-treated GBM cells, whereas NES < 0 indicates downregulated biological processes.

Tumor dissociation for scRNA-seq. G411-bearing NSG mice treated with either K59-78^{TAT} or K90-114^{TAT} were processed for scRNA-seq. Ten days after peptide treatment, three mice from each group were anesthetized and perfused with DPBS. GFP$^+$ tumors were dissected under a fluorescent dissection scope and dissociated with the Papain dissociation system (Worthington, no. LK003150). Sample quality control, library preparation and sequencing were performed by The Center for Applied Genomics, The Hospital for Sick Children, Toronto, Canada.

scRNA-seq. Raw scRNA-seq data were mapped to the combined mm10 and hg38 reference genomes to identify specific murine and human cancer cell transcrips using the CellRanger toolkit (v.4.0.0). To remove the batch effect of experiments, the cellranger aggr function was applied to integrate gene expression matrices. Cells containing at

least 90% human and mouse genome reads were considered as human and mouse cells, respectively. Cells that did not meet these criteria were considered as human–mouse multiplets and were removed from subsequent analysis.

Gene-barcode count matrices were analyzed with the R package Seurat (v.4.0.3). Cells with either <500 or >8,000 genes detected were excluded because of low quality and potential doublets. In addition, cells with >10% mitochondrial gene mapped reads were also filtered. In total, 18,454 patient-derived xenograft (PDX) GBM cells and 1,202 mouse cells were retained for further analysis in Seurat object. Following quality control, scRNA-seq datasets were log normalized and dimensionality reduced by principal component analysis. With the Elbowplot function in Seurat, the top 25 principal components were selected as input for generation of UMAP plots. Cell clusters were identified by performing *k*-nearest neighbor unsupervised clustering, with resolution set at 1.2. Conventional markers described in previous research and the inferCNV (v.1.8.0) algorithm were used to categorize every cluster into a known biological cell type. Subsequently, tumor cells were subset and further clustered into subclusters to detect heterogeneity within cell type. The Seurat Findallmarker function was used to identify preferentially expressed genes in clusters or differentially expressed genes between different conditions. When the expression of a particular feature exceeded the average expression of that feature in the entire cell population, we defined that cell as a 'feature-expressing cell'.

Gene set enrichment analysis. Gene sets (including axon, axonogenesis, neuron, synapse and neuronal projection-related genesets) from MSigDB were downloaded and used to estimate the biological activity in each cell through the R package AUCell (v.1.14.0). Cluster 7 signature was selected from the Findallmarker results with $\log_2(FC) > 0.5$ and $P < 0.05$. The ssGSEA algorithm in the R package GSVA (v.1.40.1) was applied to estimate enrichment of the siganture in bulk transcript datasets. All calculated scores were scaled to range 0–1. In addition, the enrichment results of GO among differentially expressed genes were generated by the R package clusterProfiler (v.4.7.1).

Survival analysis. The median of every feature was used as cutoff to analyze the relationship between expression level and overall survival. Hazard ratios with 95% confidence intervals, log-rank *P* values and Kaplan–Meier curves were calculated and plotted with the R packages survival (v.3.2-11) and survminer (v.0.4.9).

Microarray analysis. Raw CEL files were background corrected and normalizd through the RMA function in the R package oligo (v.1.56.0). We selected GBM-482 and GBM-472 cells to detect differentially expressed genes between TMZ-sensitive and -resistant clones using the R package limma (v.3.48.0). Differentially expressed genes with FDR < 0.05 and $|\log_2(FC)| > 0.5$ were accepted as significant.

Statistics and reproducibility

The statistical tests used are indicated in the accompanying figure legends. All findings were considered significant at a *P* value threshold of 0.05. Significant *P* values are indicated within figures. Data distribution was assumed to be normal, but this was not formally tested. Based on the variance of xenograft tumor growth in control mice, power calculations indicated that the use of at least three mice per group would give 80% power to detect an effect size of 20% with a significance level of 0.05. We used a minimum of five animals per experimental group to detect differences among groups with a large magnitude of effects. Statistical methods were not used to predetermine sample sizes for other experiments, but our sample sizes are similar to those reported in previous publications[13,14]. Three biologically independent samples were used for bulk RNA-seq and scRNA-seq due to the considerations of labor, time and cost. For immunohistochemistry studies, at least three independent samples were studied and at least three spatially distinct regions per sample were studied to verify reproducibility. All other experiments were conducted with at least three biologically independent replicates. Mice with comparable tumor burdens were randomly assigned into different experimental groups. This strategy ensures comparable mean tumor burden in each group before treatment. Data collection was randomized or appropriately blocked and samples were randomly allocated into each experimental group when possible. Animals were monitored and endpoints were called by veterinary technicians who were unaware of our experimental settings. Data were collected and analyzed by the same person, so blinding was not possible. No data were excluded from analyses.

Ethical statement

Patient-derived GBM cell lines were generated from patient tumor samples during their operative procedure following informed consent. All experimental procedures were performed in accordance with the Research Ethics Board at The Hospital for Sick Children (Toronto, Canada). All primary human fetal cells were obtained from the Research Centre for Women's and Infants' Health BioBank (Toronto, Canada) and Mount Sinai Hospital (Toronto, Canada).

All procedures involving animals were performed in compliance with the Animals for Research Act of Ontario and the Guidelines of the Canadian Council on Animal Care. The Centre for Phenogenomics Animal Care Committee reviewed and approved all procedures conducted. Humane intervention points/scientific endpoints would typically be based on clinical signs for brain tumors as per SOP no. AH009 Cancer Models—Humane Intervention Point Guidelines, and not necessarily on tumor size/burden. All mice were humanely killed before or at the intervention points/scientific endpoints.

Reporting summary

Further information on research design is available in the Nature Portfolio Reporting Summary linked to this article.

Data availability

The spatial expression of EAG2, Kvβ2 and other genes in GBM geometrical regions was derived from the Ivy Glioblastoma Atlas Project (https://glioblastoma.alleninstitute.org). The structure of Kvβ2 is available at the Protein Data Bank with accession code 3eau (https://www.ebi.ac.uk/pdbe/entry/pdb/3eau). IlluminaHiseq RNA-seq data of The Cancer Genome Atlas LGGs and GBMs are available at NCI's Genomic Data Commons (https://gdc.cancer.gov/about-data/publications/lgggbm_2016). The clinical information and gene expression datasets of CGGA (mRNAseq_693, Illumina HiSeq) are available at the Chinese Glioma Genome Atlas (http://www.cgga.org.cn/index.jsp). Previously published microarray data of TMZ-resistant and -sensitive GBM clones that were reanalyzed here are available at ArrayExpress under accession code E-MTAB-2693 (https://www.ebi.ac.uk/arrayexpress/experiments/E-MTAB-2693/). Preprocessed transcript data from the GLASS Consortium are available at Synapse (https://www.synapse.org/glass). Bulk RNA-seq data from GBM cell–neuron coculture, and scRNA-seq data from the PDX GBM model with peptide treatment reported in this manuscript, have been deposited in the NCBI Gene Expression Omnibus under accession code GSE231577. All unique materials such as patient-derived cell cultures are freely available and can be obtained by contacting the corresponding author and with a standard material transfer agreement with The Hospital for Sick Children. Data for all figures can be found within the manuscript, in the accompanying source data or from the corresponding author on reasonable request. Source data are provided with this paper.

Code availability

All codes used in this manuscript are freely available at GitHub (https://github.com/l-magnificence/Sequencing-Data-Analysis-Code-for-EAG2-Project).

References

1. Kotecha, R., Odia, Y., Khosla, A. A. & Ahluwalia, M. S. Key clinical principles in the management of glioblastoma. *JCO Oncol. Pract.* **19**, 180–189 (2023).
2. Stupp, R. et al. Radiotherapy plus concomitant and adjuvant temozolomide for glioblastoma. *N. Engl. J. Med.* **352**, 987–996 (2005).
3. Lee, S. Y. Temozolomide resistance in glioblastoma multiforme. *Genes Dis.* **3**, 198–210 (2016).
4. Johnson, B. E. et al. Mutational analysis reveals the origin and therapy-driven evolution of recurrent glioma. *Science* **343**, 189–193 (2014).
5. van Thuijl, H. F. et al. Evolution of DNA repair defects during malignant progression of low-grade gliomas after temozolomide treatment. *Acta Neuropathol.* **129**, 597–607 (2015).
6. Pan, Y. et al. NF1 mutation drives neuronal activity-dependent initiation of optic glioma. *Nature* **594**, 277–282 (2021).
7. Chen, P. et al. Olfactory sensory experience regulates gliomagenesis via neuronal IGF1. *Nature* **606**, 550–556 (2022).
8. Magnon, C. et al. Autonomic nerve development contributes to prostate cancer progression. *Science* **341**, 1236361 (2013).
9. Venkatesh, H. S. et al. Neuronal activity promotes glioma growth through neuroligin-3 secretion. *Cell* **161**, 803–816 (2015).
10. Venkatesh, H. S. et al. Targeting neuronal activity-regulated neuroligin-3 dependency in high-grade glioma. *Nature* **549**, 533–537 (2017).
11. Dolma, S. et al. Inhibition of dopamine receptor D4 impedes autophagic flux, proliferation, and survival of glioblastoma stem cells. *Cancer Cell* **29**, 859–873 (2016).
12. Hayakawa, Y. et al. Nerve growth factor promotes gastric tumorigenesis through aberrant cholinergic signaling. *Cancer Cell* **31**, 21–34 (2017).
13. Venkataramani, V. et al. Glutamatergic synaptic input to glioma cells drives brain tumour progression. *Nature* **573**, 532–538 (2019).
14. Venkatesh, H. S. et al. Electrical and synaptic integration of glioma into neural circuits. *Nature* **573**, 539–545 (2019).
15. Curry, R. N. et al. Glioma epileptiform activity and progression are driven by IGSF3-mediated potassium dysregulation. *Neuron* **111**, 682–695 (2023).
16. Zeng, Q. et al. Synaptic proximity enables NMDAR signalling to promote brain metastasis. *Nature* **573**, 526–531 (2019).
17. Anastasaki, C., Gao, Y. & Gutmann, D. H. Neurons as stromal drivers of nervous system cancer formation and progression. *Dev. Cell* **58**, 81–93 (2023).
18. Winkler, F. et al. Cancer neuroscience: state of the field, emerging directions. *Cell* **186**, 1689–1707 (2023).
19. Osswald, M. et al. Brain tumour cells interconnect to a functional and resistant network. *Nature* **528**, 93–98 (2015).
20. Yu, K. et al. PIK3CA variants selectively initiate brain hyperactivity during gliomagenesis. *Nature* **578**, 166–171 (2020).
21. Krishna, S. et al. Glioblastoma remodelling of human neural circuits decreases survival. *Nature* **617**, 599–607 (2023).
22. Hille, B. *Ion Channels of Excitable Membranes* 3rd edn (Sinauer, 2001).
23. Bagal, S. K. et al. Ion channels as therapeutic targets: a drug discovery perspective. *J. Med. Chem.* **56**, 593–624 (2013).
24. Hutchings, C. J., Colussi, P. & Clark, T. G. Ion channels as therapeutic antibody targets. *MAbs* **11**, 265–296 (2019).
25. Pongs, O. & Schwarz, J. R. Ancillary subunits associated with voltage-dependent K+ channels. *Physiol. Rev.* **90**, 755–796 (2010).
26. Liu, X., Chang, Y., Reinhart, P. H., Sontheimer, H. & Chang, Y. Cloning and characterization of glioma BK, a novel BK channel isoform highly expressed in human glioma cells. *J. Neurosci.* **22**, 1840–1849 (2002).
27. Sales, T. T. et al. Suppression of the Eag1 potassium channel sensitizes glioblastoma cells to injury caused by temozolomide. *Oncol. Lett.* **12**, 2581–2589 (2016).
28. Venturini, E. et al. Targeting the potassium channel Kv1.3 kills Glioblastoma cells. *Neurosignals* **25**, 26–38 (2017).
29. Puchalski, R. B. et al. An anatomic transcriptional atlas of human glioblastoma. *Science* **360**,660–663 (2018).
30. Varn, F. S. et al. Glioma progression is shaped by genetic evolution and microenvironment interactions. *Cell* **185**, 2184–2199 (2022).
31. Weil, S. et al. Tumor microtubes convey resistance to surgical lesions and chemotherapy in gliomas. *Neurol. Oncol.* **19**, 1316–1326 (2017).
32. Park, N. I. et al. ASCL1 reorganizes chromatin to direct neuronal fate and suppress tumorigenicity of glioblastoma stem cells. *Cell Stem Cell* **21**, 209–224 (2017).
33. Hamed, A. A. et al. A brain precursor atlas reveals the acquisition of developmental-like states in adult cerebral tumours. *Nat. Commun.* **13**, 4178 (2022).
34. Pan, Y. et al. Cortisone dissociates the Shaker family K^+ channels from their beta subunits. *Nat. Chem. Biol.* **4**, 708–714 (2008).
35. Magill, S. T., Choy, W., Nguyen, M. P. & McDermott, M. W. Ommaya reservoir insertion: a technical note. *Cureus* **12**, e7731 (2020).
36. Uetani, N., Chagnon, M. J., Kennedy, T. E., Iwakura, Y. & Tremblay, M. L. Mammalian motoneuron axon targeting requires receptor protein tyrosine phosphatases sigma and delta. *J. Neurosci.* **26**, 5872–5880 (2006).
37. Suto, F. et al. Plexin-a4 mediates axon-repulsive activities of both secreted and transmembrane semaphorins and plays roles in nerve fiber guidance. *J. Neurosci.* **25**, 3628–3637 (2005).
38. Rosenstein, J. M., Krum, J. M. & Ruhrberg, C. VEGF in the nervous system. *Organogenesis* **6**, 107–114 (2010).
39. McGregor, C. E. & English, A. W. The role of BDNF in peripheral nerve regeneration: activity-dependent treatments and Val66Met. *Front. Cell Neurosci.* **12**, 522 (2018).
40. Yoon, C. et al. Low-density lipoprotein receptor-related protein 1 (LRP1)-dependent cell signaling promotes axonal regeneration. *J. Biol. Chem.* **288**, 26557–26568 (2013).
41. Goldshmit, Y. et al. EphA4 blockers promote axonal regeneration and functional recovery following spinal cord injury in mice. *PLoS ONE* **6**, e24636 (2011).
42. Sanchez-Huertas, C. et al. The +TIP Navigator-1 is an actin-microtubule crosslinker that regulates axonal growth cone motility. *J. Cell Biol.* https://doi.org/10.1083/jcb.201905199 (2020).
43. Li, H. et al. Transcription factor MEF2C influences neural stem/progenitor cell differentiation and maturation in vivo. *Proc. Natl Acad. Sci. USA* **105**, 9397–9402 (2008).
44. Ohkubo, Y., Uchida, A. O., Shin, D., Partanen, J. & Vaccarino, F. M. Fibroblast growth factor receptor 1 is required for the proliferation of hippocampal progenitor cells and for hippocampal growth in mouse. *J. Neurosci.* **24**, 6057–6069 (2004).
45. Liu, X. et al. Effect of Spp1 on nerve degeneration and regeneration after rat sciatic nerve injury. *BMC Neurosci.* **18**, 30 (2017).
46. Kim, Y. et al. Perspective of mesenchymal transformation in glioblastoma. *Acta Neuropathol. Commun.* **9**, 50 (2021).
47. Meyer, M. et al. Single cell-derived clonal analysis of human glioblastoma links functional and genomic heterogeneity. *Proc. Natl Acad. Sci. USA* **112**, 851–856 (2015).
48. Wang, H. et al. LGALS3 promotes treatment resistance in glioblastoma and is associated with tumor risk and prognosis. *Cancer Epidemiol. Biomarkers Prev.* **28**, 760–769 (2019).
49. Venkataramani, V. et al. Disconnecting multicellular networks in brain tumours. *Nat. Rev. Cancer* **22**, 481–491 (2022).
50. Huang, X. et al. Voltage-gated potassium channel EAG2 controls mitotic entry and tumor growth in medulloblastoma via regulating cell volume dynamics. *Genes Dev.* **26**, 1780–1796 (2012).

51. Monje, M. et al. Roadmap for the emerging field of cancer neuroscience. *Cell* **181**, 219–222 (2020).
52. Venkataramani, V., Tanev, D. I., Kuner, T., Wick, W. & Winkler, F. Synaptic input to brain tumors: clinical implications. *Neurol. Oncol.* **23**, 23–33 (2021).
53. Huang, X. et al. EAG2 potassium channel with evolutionarily conserved function as a brain tumor target. *Nat. Neurosci.* **18**, 1236–1246 (2015).
54. Francisco, M. A. et al. Chloride intracellular channel 1 cooperates with potassium channel EAG2 to promote medulloblastoma growth. *J. Exp. Med.* https://doi.org/10.1084/jem.20190971 (2020).
55. Serrano-Heras, G. et al. Involvement of N-methylpurine DNA glycosylase in resistance to temozolomide in patient-derived glioma cells. *Sci. Rep.* **10**, 22185 (2020).
56. Huang, L. et al. Inhibition of intermedin (adrenomedullin 2) suppresses the growth of glioblastoma and increases the antitumor activity of temozolomide. *Mol. Cancer Ther.* **20**, 284–295 (2021).
57. Aarts, M. et al. Treatment of ischemic brain damage by perturbing NMDA receptor–PSD-95 protein interactions. *Science* **298**, 846–850 (2002).
58. Cook, D. J., Teves, L. & Tymianski, M. A translational paradigm for the preclinical evaluation of the stroke neuroprotectant Tat-NR2B9c in gyrencephalic nonhuman primates. *Sci. Transl. Med.* **4**, 154ra133 (2012).

Acknowledgements

This work is supported by the SickKids Foundation, Arthur and Sonia Labatt Brain Tumour Research Centre, Garron Family Cancer Centre, Canadian Cancer Society Challenge Grant, Concern Foundation Conquer Cancer Now Award, b.r.a.i.n.child, Sontag Foundation Distinguished Scientist Award, Meagan's HUG, Natural Sciences and Engineering Research Council Discovery Grant, Ontario Institute for Cancer Research Translational Research Initiative, Early Researcher Award and Canadian Institute of Health Research Project Grants (to X.H.), a Garron Family Cancer Centre Pitblado Discovery Grant (to L.-Y.W. and X.H.), Canadian Institute of Health Research Project Grants PJT-156034 and PJT-156439 and a Natural Sciences and Engineering Research Council grant RGPIN-2017-06665 (to L.-Y.W.). Xin C. is supported by SickKids Restracomp Scholarship. S.B. is supported by an International Postdoc Grant from the Swedish Research Council (Vetenskapsrådet) and Powered by Pablove Research Grant from Pablove Foundation. We thank J. Lathia for sharing GL261 cells, S. O. Kelley for sharing PC9 and H1975 cells and J. Ellis for sharing HEK293T cells, human astrocytes and lentivirus packaging plasmids. We thank P. Paroutis and K. Lau at SickKids Imaging Facility for help with confocal imaging and image analysis. We thank C. Simpson at SickKids SPARC BioCentre Molecular Analysis for assistance with mass spectrometry experiments. We thank the staff at The Centre for Phenogenomic for their help on animal works. We thank W. Wang for technical assistance and Huang laboratory members for comments on the manuscript. Schematics in Figs. 2a, 5c,e, 7a and 8 created with BioRender.com. X.H. is a Catalyst Scholar at The Hospital for Sick Children and Canada Research Chair in Cancer Biophysics.

Author contributions

X.H. directed the study. Experimental design, data acquisition and data analysis were carried out by W.D., A.F., Xiaodi C., H.L., G.L.B., Xin C., S.B., Y.X., Q.Y., H.Z., T.K., M.S.M., G.J., J.-E.K., G.J., Y.S., T.-H.K., Y.H., S.W., X.L., R.A.M. and L.-Y.W. Reagent contributions were provided by D.S. and P.B.D. W.D. and X.H. wrote the manuscript.

Competing interests

W.D. and X.H. have filed a PCT patent for the composition of matter and use of designer peptides to treat cancer. The remaining authors declare no competing interests.

Additional information

Extended data is available for this paper at https://doi.org/10.1038/s43018-023-00626-8.

Supplementary information The online version contains supplementary material available at https://doi.org/10.1038/s43018-023-00626-8.

Correspondence and requests for materials should be addressed to Xi Huang.

Peer review information *Nature Cancer* thanks Justin Lathia, Stephen Robbins and Harald Sontheimer for their contribution to the peer review of this work.

Reprints and permissions information is available at www.nature.com/reprints.

Publisher's note Springer Nature remains neutral with regard to jurisdictional claims in published maps and institutional affiliations.

[1]Developmental and Stem Cell Biology Program, The Hospital for Sick Children, Toronto, Ontario, Canada. [2]Arthur and Sonia Labatt Brain Tumour Research Centre, The Hospital for Sick Children, Toronto, Ontario, Canada. [3]Department of Molecular Genetics, University of Toronto, Toronto, Ontario, Canada. [4]Neurosciences and Mental Health Program, The Hospital for Sick Children, Toronto, Ontario, Canada. [5]Department of Neurosurgery, Xiangya Hospital, Central South University, Changsha, China. [6]Hunan International Scientific and Technological Cooperation Base of Brain Tumor Research, Xiangya Hospital, Central South University, Changsha, China. [7]Molecular Medicine Program, The Hospital for Sick Children, Toronto, Ontario, Canada. [8]Department of Physiology, University of Toronto, Toronto, Ontario, Canada. [9]Macaulay Honors College, City College of New York, New York, NY, USA. [10]Advanced Science Research Center at the Graduate Center, City University of New York, New York, NY, USA. [11]The Raymond G. Perelman Center for Cellular and Molecular Therapeutics, The Children's Hospital of Philadelphia, Philadelphia, PA, USA. [12]Department of Pathology and Laboratory Medicine, University of Pennsylvania, Philadelphia, PA, USA. [13]Centre for Molecular and Systems Biology, Lunenfeld-Tanenbaum Research Institute, Mount Sinai Hospital, Toronto, Ontario, Canada. [14]Department of Biochemistry, University of Toronto, Toronto, Ontario, Canada. ✉e-mail: xi.huang@sickkids.ca

https://doi.org/10.1038/s43018-023-00626-8

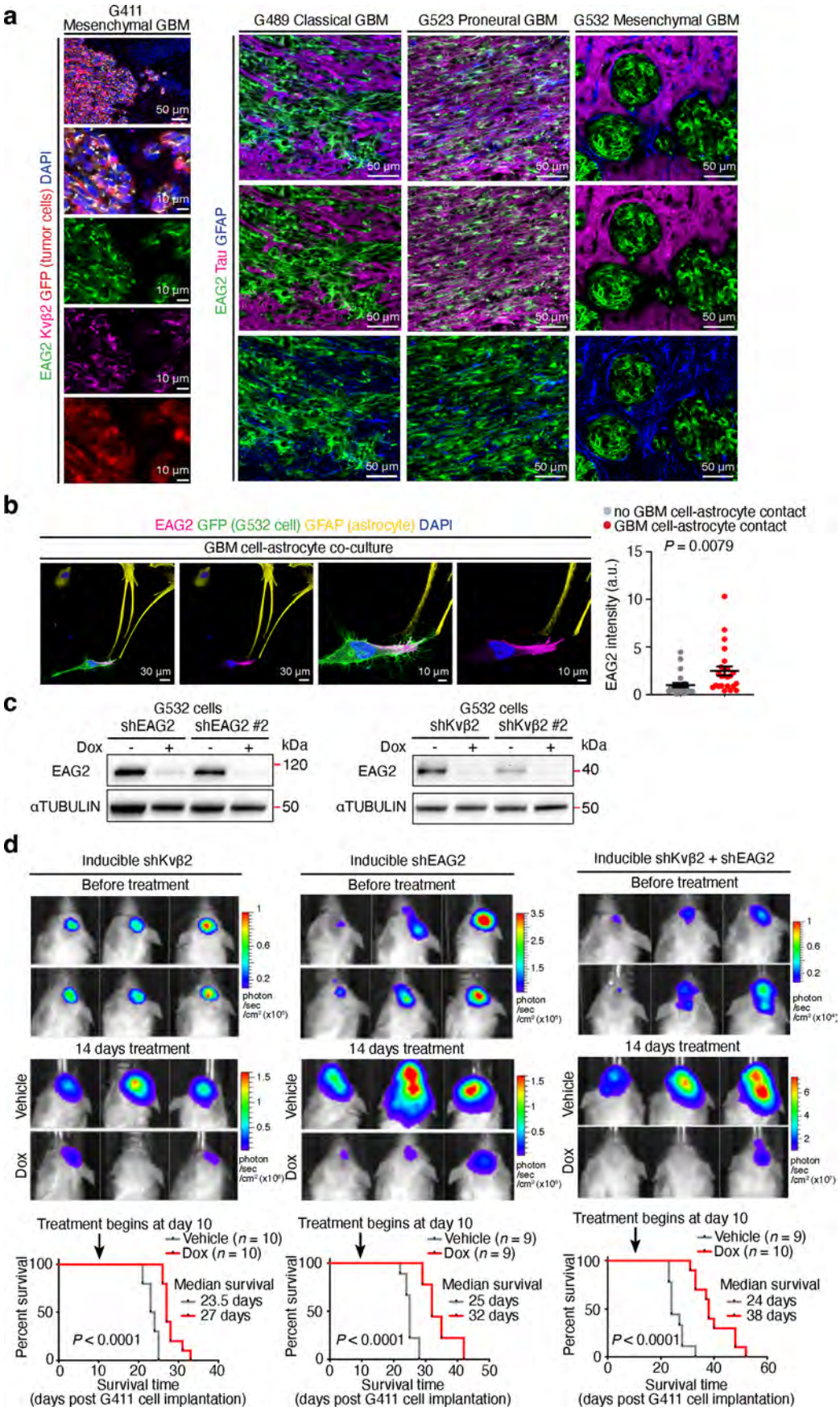

Extended Data Fig. 1 | See next page for caption.

https://doi.org/10.1038/s43018-023-00626-8

Extended Data Fig. 1 | EAG2 and Kvβ2 expression in xenograft GBM tumors, EAG2 localization in GBM cells, EAG2 and Kvβ2 knockdown validation, and tumor growth comparison between control tumor and tumor with knockdown of EAG2, Kvβ2, or both. a. EAG2, Kvβ2, GFP, and DAPI expression in G411 xenograft tumor. EAG2, Tau, and GFAP expression in G489, G523, and G532 xenograft tumors. **b**. Representative images and quantification of EAG2 localization in GBM cells with or without contact of astrocytes. $n = 24$ cells examined over 3 independent experiments. *P* values, two-sided unpaired *t*-test. Error bars, mean ± s.e.m. **c**. Validation of Dox-induced knockdown of EAG2 and Kvβ2. **d**. Bioluminescence images show tumor burdens of mice bearing G411 tumors before and after Dox treatment. Kaplan-Meier survival curves are shown. *P* values, log-rank test. All experiments were performed 3 times using biologically independent samples.

https://doi.org/10.1038/s43018-023-00626-8

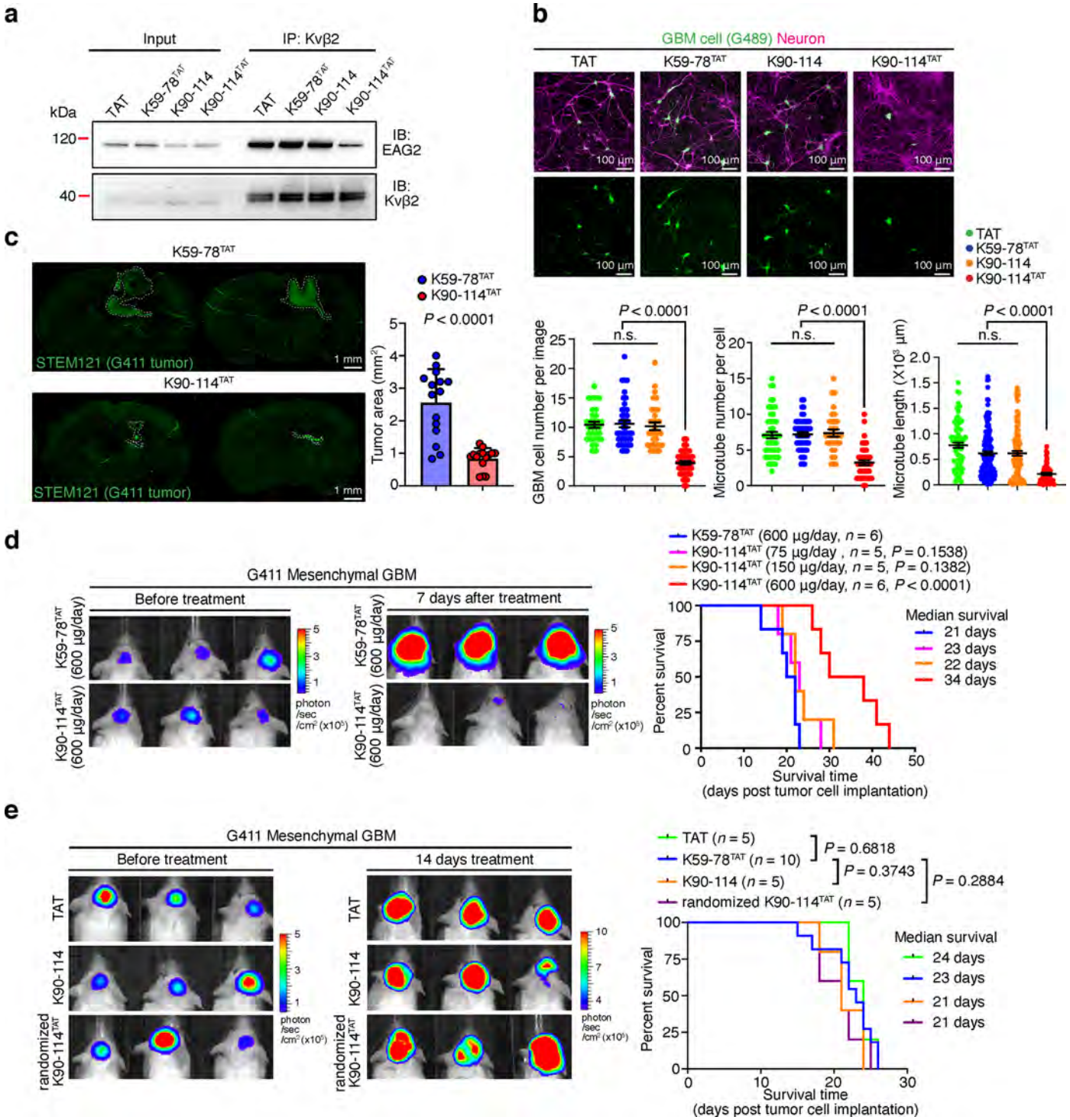

Extended Data Fig. 2 | Characterization of peptide treatment on GBM cell growth *in vitro* and tumor growth *in vivo*. **a**. Co-IP shows EAG2-Kvβ2 interaction in G411 GBM cells treated with TAT, K59-78^{TAT}, K90-114, or K90-114^{TAT}. 3 biologically independent experiments were performed. **b**. Cell number, microtube number per cell, and microtube length of G489 GBM cells, which are co-cultured with neurons, after TAT, K59-78^{TAT}, K90-114, or K90-114^{TAT} treatment. Sample size (from left to right): n = 31, 42, 31, 43, 50, 52, 33, 41, 78, 146, 116, 49 cells examined over 3 independent experiments. Adjusted P value was calculated by Tukey's multiple comparisons test (n.s. means not significant, $P > 0.05$). Error bars, mean ± s.e.m. Cell number and microtube length of K59-78^{TAT} and K90-114^{TAT} treated cells are also shown in Fig. 5b for easier data interpretation. **c**. Representative images and quantification of tumor areas of G411 xenograft tumors treated for 7 days with K59-78^{TAT} or K90-114^{TAT}. n = 15 samples examined from 5 biologically independent animals. P values, two-sided unpaired t-test. Error bars, mean ± s.e.m. **d**. Bioluminescence images and survival comparison of G411 GBM-bearing mice treated with K59-78^{TAT} or K90-114^{TAT} at various dosages. P values, log-rank test. Each P value was generated individually by comparing to K59-78^{TAT}. **e**. Bioluminescence images and survival comparison of G411 GBM-bearing mice treated with TAT, K90-114, or randomized K90-114 ^{TAT}. K59-78^{TAT} survival curve is derived from Fig. 5d. P values, log-rank test.

https://doi.org/10.1038/s43018-023-00626-8

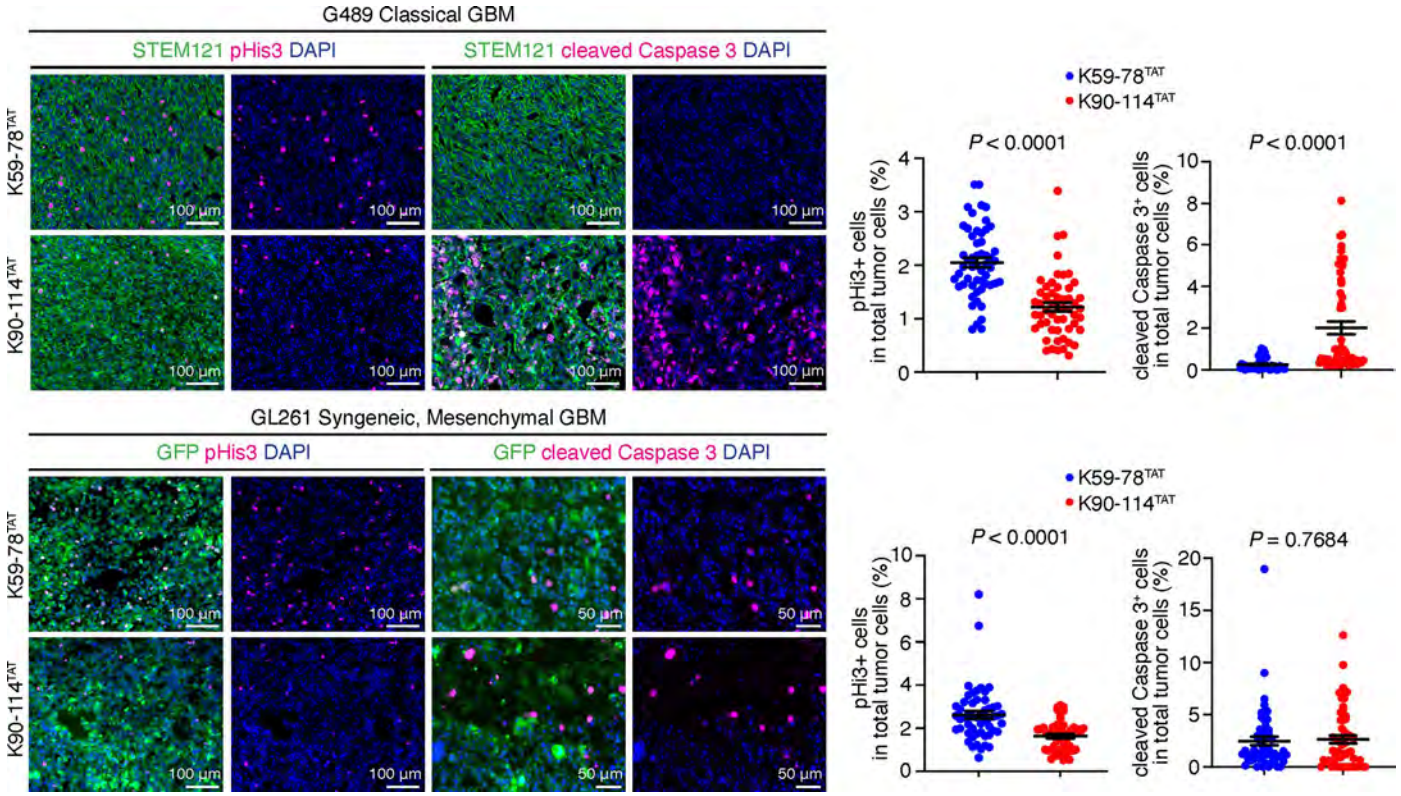

Extended Data Fig. 3 | K90-114^{TAT} treatment alters proliferation and apoptosis of GBM tumors. Representative images showing proliferation and apoptosis of G489 xenograft tumors (pHis3: $n = 54$, cleaved caspase 3: $n = 53$) or GL261 syngeneic tumors (pHis3: $n = 53$ and 48, cleaved caspase 3: $n = 54$) treated with K59-78^{TAT} or K90-114^{TAT}. STEM121 labels G489 tumor cells. GFP labels GL261 tumor cells. pHis3 labels mitotic cells. cleaved caspase 3 labels apoptotic cells. Samples were evenly and independently collected from 3 animals. *P* values, two-sided unpaired *t*-test. Error bars, mean ± s.e.m.

https://doi.org/10.1038/s43018-023-00626-8

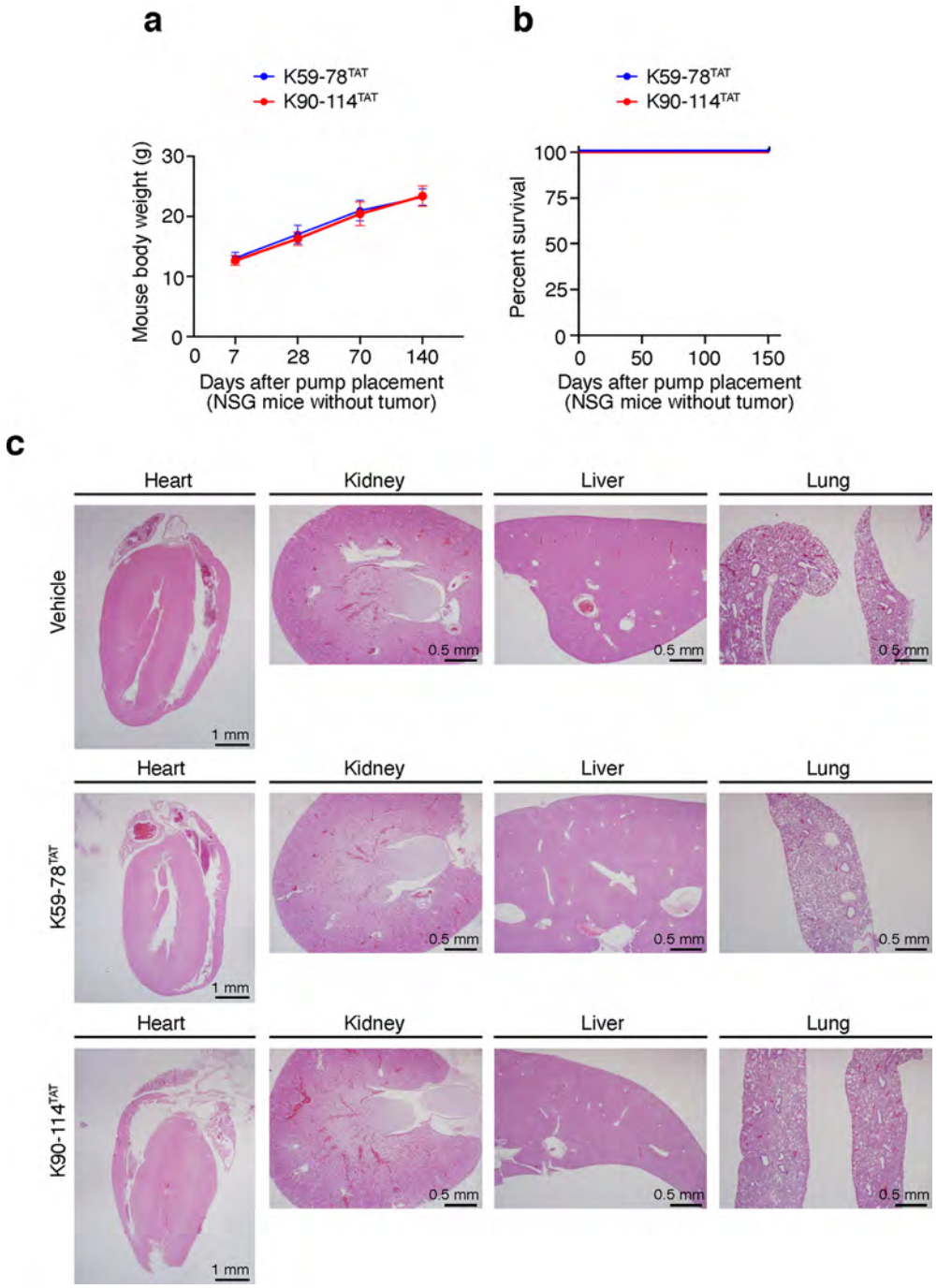

Extended Data Fig. 4 | K90-114^{TAT} treatment does not affect mouse body weight, survival, and internal organs. a. Body weight of K59-78^{TAT}- and K90-114^{TAT}-treated tumor-free NSG mice (n = 9 mice in each group). **b**. Survival of K59-78^{TAT}- and K90-114^{TAT}-treated tumor-free NSG mice (n = 9 mice in each group). **c**. Pathological analysis of hearts, kidneys, livers, and lungs harvested from control, K59-78^{TAT} and K90-114^{TAT}-treated tumor-bearing NSG mice (n = 3 mice in each group).

https://doi.org/10.1038/s43018-023-00626-8

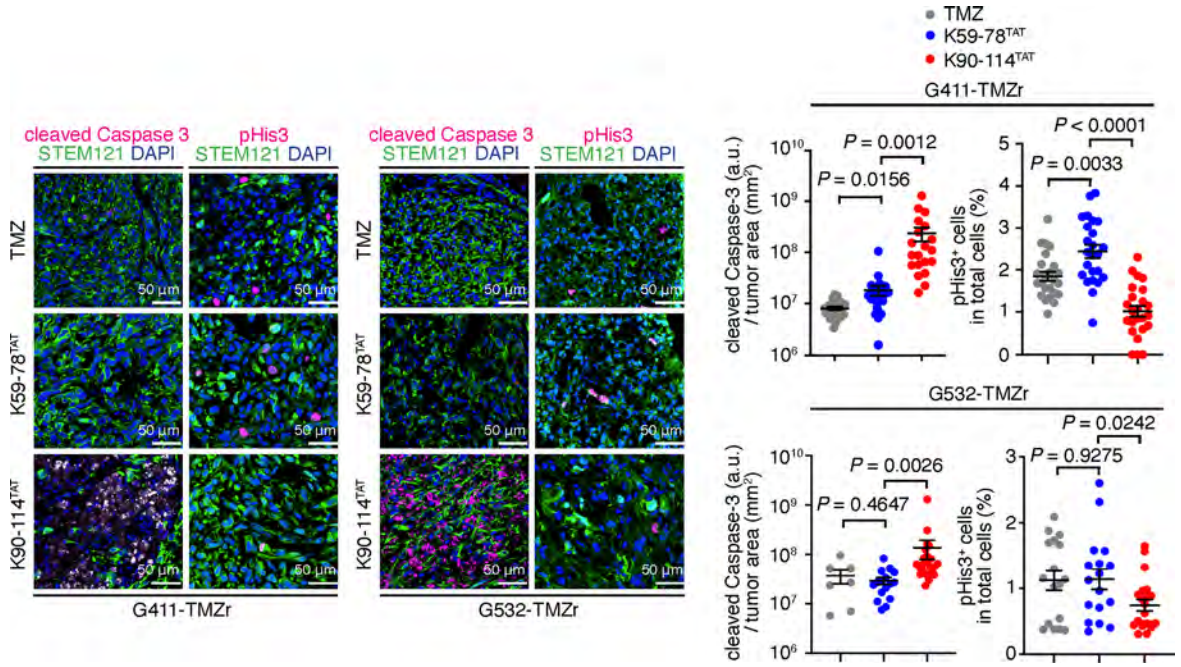

Extended Data Fig. 5 | K90-114^{TAT} treatment decreases proliferation and increases apoptosis of TMZ-resistant GBM. Representative images showing STEM121^{+} tumor cells, pHis3^{+} mitotic cells, and cleaved caspase 3^{+} apoptotic cells in TMZ-resistant xenograft tumors treated with TMZ, K59-78^{TAT} and K90-114^{TAT}. Sample size (from left to right): G411-TMZr: n = 24, 25, 21, 24, 24, 24; G532-TMZr: n = 7, 15, 21, 17, 17, 21. Samples were evenly and independently collected from 3 animals. P values, two-sided unpaired t-test. Error bars, mean ± s.e.m.